practice guide

X-Ray Topography

0.5 mm

David R. Black
Gabrielle G. Long

960-10

Special
Publication
960-10

Certain commercial entities, equipment, or materials may be identified in
this document in order to describe an experimental procedure or concept
adequately. Such identification is not intended to imply recommendation or
endorsement by the National Institute of Standards and Technology, nor is it
intended to imply that the entities, materials, or equipment are necessarily the
best available for the purpose.

FOREWORD

The study of the interrelationships between processing, structure and properties of materials is fundamental to the field of materials science and engineering. The need to understand the microstructure of materials has driven the development of a wide variety of x-ray based characterization techniques. While X-ray topography is a very powerful tool for the evaluation of crystals for technological applications and for many areas of crystal and thin-film growth and processing, it is perhaps less well known and, therefore, has historically been underutilized in the United States. The aim of this guide is to raise the awareness of X-ray topography and, therefore, make modern x-ray topography techniques more accessible to materials scientists who would benefit by obtaining the rich variety of microstructural information it offers. The basic principles and practical aspects of topography are discussed and demonstrated through examples to help illustrate the diverse applications of this technique.

ACKNOWLEDGMENTS

TABLE OF CONTENTS

List of Figures

1. INTRODUCTION

X-ray topography (XRT) is a nondestructive characterization technique for imaging, by means of X-ray diffraction, the micrometer-sized to centimeter-sized defect microstructure of crystals. Topography got its name from the fact that the diffraction image can resemble a geographical topographic map with the appearance of different elevations and topographical contours. However, since diffracted X-rays form the image, its interpretation is not always straightforward. XRT is a very powerful tool for the evaluation of crystals for technological applications and for characterizing crystal and thin-film growth and processing. The aim of this guide is to make modern X-ray topography more accessible to materials scientists and others who would benefit from the rich variety of microstructural information that it offers.

In X-ray topography, the crystal sample is illuminated by an X-ray beam and images of the diffracted beams are recorded. These images are generally formed from X-ray wave fields interfering with one another inside the crystal. The image from a perfect crystal is usually completely homogeneous. Changes in the image contrast are seen if there are imperfections in the crystal which cause deviations, *u(r),* from perfect long-range atomic order. In most cases, the defects themselves are not visible in the image, but rather the lattice deformations surrounding the defects are seen. An X-ray topograph of a diamond crystal, shown in Figure 1, displays four of the defects most commonly observed in X-ray topographs: dislocations, stacking faults, inclusions, and surface damage. Later, examples are given to illustrate the wide range of applications for which topography is used to characterize crystals.
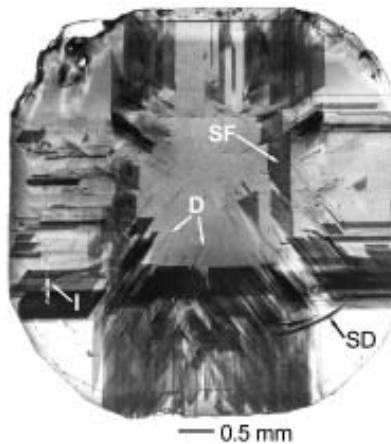
Figure 1. *A ($\bar{1}$11) transmission topograph of an isotopically-pure diamond crystal, approximately 0.75 mm thick, showing four of the defects commonly seen in X-ray topography,* e.g.*, individual dislocations (D), stacking faults (SF), inclusions (I), and surface damage (SD).*

At modern synchrotron X-ray sources, microstructural evolution can be observed on X-ray-sensitive video cameras in real time with subsecond resolution, *e.g.*, to follow the kinetics of defect motion, phase transitions, and crystal growth. Depending on the optical parameters of the experiment, the strain sensitivity can approach $\Delta d/d \sim 10^{-8}$ (where d is the lattice spacing), the sensitivity to crystal orientation can be a few µrad, the spatial resolution can approach 1 µm, and sample areas as large as 100 cm^2 can be imaged in a single exposure.

In the reflection (Bragg) geometry, an X-ray topograph emphasizes the microstructure of the surface region (typically within 1 µm − 10 µm) of the crystal surface. In the transmission (Laue) geometry, an X-ray topograph displays the bulk microstructure of the crystal. For reasonably good crystals (what this means will be discussed later), a transmitted diffraction image can be recorded through several millimeters of material. Information that can be extracted from topographs includes: the density and distribution of dislocations (including Burgers vector analysis), the distribution of inhomogeneous strain (caused, for example, by thermal processing or a variation in impurity concentration), subgrain structures including misorientation angles, the depth of defects below the surface, and the presence of voids, secondary phases and twins. In reflection and transmission topography, defect visibility depends upon the scalar product, $\boldsymbol{g} \bullet \boldsymbol{u}$, where $\boldsymbol{g}$ is the diffraction vector. This dependence can be exploited to determine the magnitude and direction of the local average atomic displacements, $\boldsymbol{u}$. [Barrett, 1945; Guinier and Tennevin, 1949; Schultz, 1954; Lang, 1958; Tanner, 1976; Boettinger, *et al.,* 1977; and Miltat, 1980].

X-ray topography, as it is practiced today, has its roots in the classical laboratory X-ray work [Berg, 1931; Barrett, 1945; Guinier and Tennevin, 1949; Shultz, 1954; Newkirk, 1958; Bonse, 1962; Lang, 1958 and 1959] of the 1930s through the 1960s. The technique was developed using characteristic radiation from laboratory X-ray sources, and much significant topography research is still done this way. [See *J. Phys. D: Applied Physics,* **28** (1995) No. 4A]. The development of synchrotron radiation sources has enabled the extension of the field by making white beam (*i.e.*, polychromatic) topography possible [Hart, 1975] and by enabling significant improvements to monochromatic XRT techniques [Tanner, 1977; Sauvage and Petroff, 1980; Kuriyama, *et al*., 1982]. This guide will discuss primarily monochromatic X-ray topography as practiced at modern synchrotron X-ray sources [See *J. Phys. D: Applied Physics,* **32** (1999) No. 10A], after a brief synopsis of the classical techniques from which it arises. Several good reviews of synchrotron radiation topography [Tanner and Bowen, 1980; Weissman, *et al.,* 1984; Lang, 1992] are available.

2. PRINCIPLES OF THE METHOD

A simple way to understand the creation of X-ray topographic images is to consider a Laue photograph [Preuss *et al.*1973]. Laue cameras are commonly used in the X-ray laboratory to orient single-crystals. (See Figure 2.)

(A)

(B)
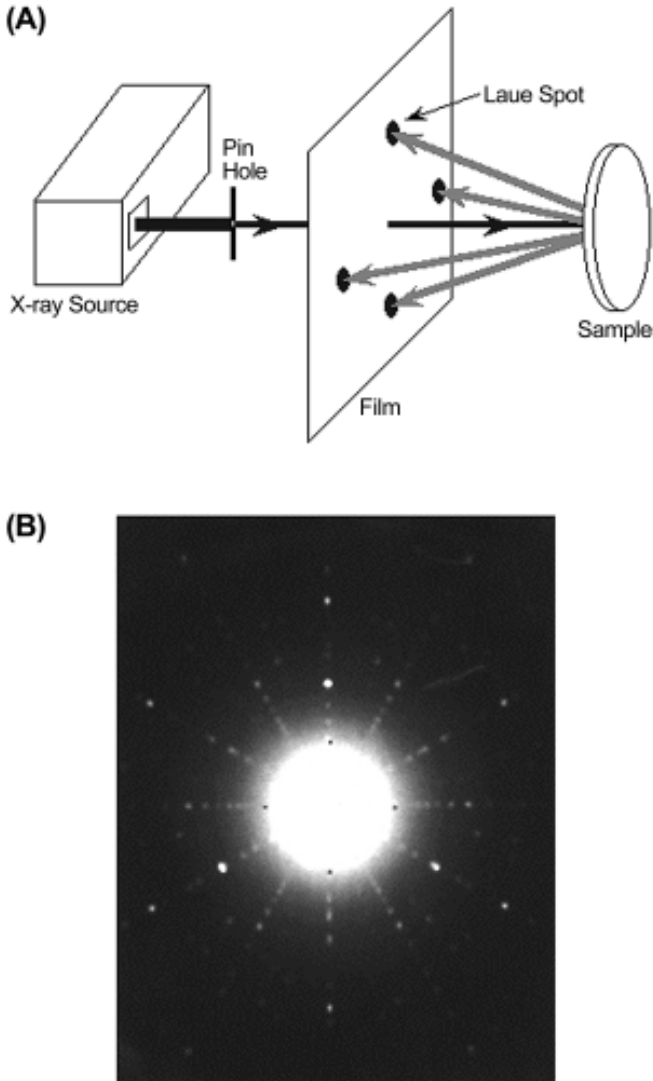
Figure 2. *A back-reflection Laue camera used to orient single crystals is shown in (A) and a typical Laue pattern is shown in (B). A divergent white X-ray beam from the laboratory source impinges the sample and the diffracted beams from a variety of lattice planes form Laue spots on the film. Because the source is divergent, the structure in the spots may be smeared.*

A polychromatic ("white") X-ray beam, containing X-ray energies from about 6 keV to 50 keV (X-ray wavelengths from approximately 2 Å to 0.25 Å), impinges on a crystal. The beam is diffracted in many directions, creating Laue spots. The positions of the diffraction spots appear according to the Bragg equation:

$$E = \frac{hc}{2d \sin \theta_B}, \qquad \text{or} \qquad \lambda = 2d \sin \theta_B, \qquad (1)$$

where E is the incident X-ray energy (and λ is the incident wavelength) selected by crystal planes with spacing d, h is Planck's constant, c is the speed of light, and θ_B is the Bragg angle. Each spot contains uniform intensity if the crystal is perfect. If, however, the crystal is strained, streaks appear instead of spots due to variations in lattice spacing, Δd. In fact, each Laue spot contains a spatial distribution of diffracted intensity attributable to the presence of defects in the crystal. This distributed intensity is difficult to see because Laue spots are typically the same size as the X-ray beam pinhole, and the incident X-ray beam is divergent, but each tiny Laue spot is actually an X-ray topograph. At synchrotron radiation facilities, a collimated white X-ray beam can be used to illuminate a sample crystal, and spots with the much larger cross section (typically 0.9 cm x 2 cm) of the synchrotron X-ray beam are recorded, Figure 3(A). The resulting data are an array of Laue spots, as shown in Figure 3(B), each of which is an X-ray topograph arising from a different set of atomic planes.

If the white synchrotron beam passes through a monochromator, an X-ray topograph is created when the sample crystal is set to the Bragg angle for a specific set of lattice planes for the selected X-ray energy. Images from different atomic planes are acquired by orienting the sample to satisfy the Bragg condition for those planes and orienting the detector to the new scattering angle ($2\theta_B$) to record the image. With monochromatic radiation only one topograph is recorded at a time, but the experimenter controls the energy or wavelength of the X-ray beam, the X-ray collimation, the energy or wavelength spread of the X-ray beam, and the size of the incident beam on the sample crystal. If the sample is large, the experimenter can enlarge the cross section of the incident beam so as to illuminate samples up to about 100 cm^2 and record the microstructure of the entire sample in a single exposure.

(A)

White Synchrotron Radiation

Sample Crystal

Projection of Vertical Diffraction Plane

Skew Topographs

Film

(B)
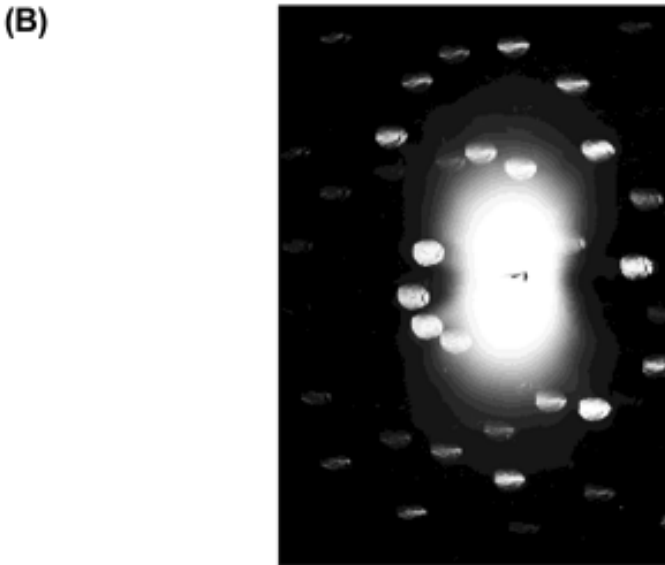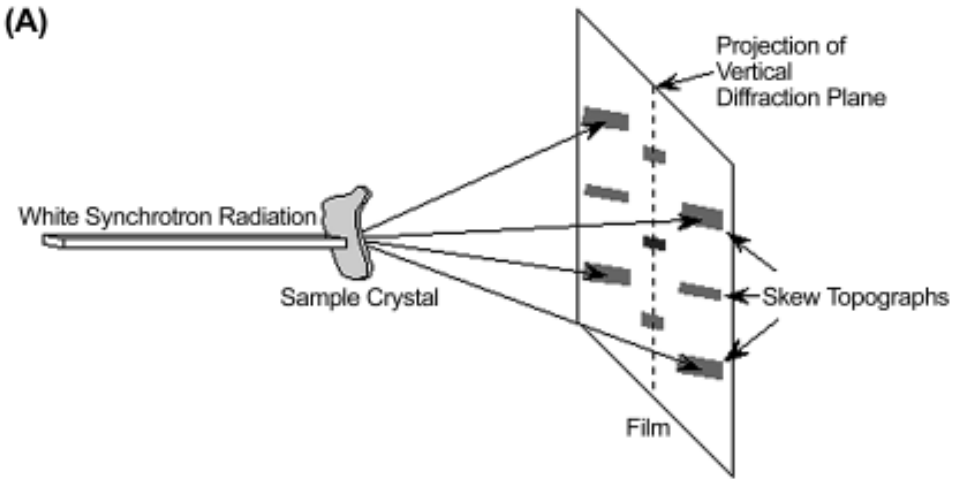
Figure 3. The geometry for white radiation topography is shown in (A) and typical images in (B). A collimated white X-ray beam from a synchrotron radiation source impinges on the sample and the diffracted beams form images on the film. It is convenient to define the principle plane of diffraction to be vertical. In general, the Laue images will not lie in the vertical plane and so will be skewed. The shape of each spot, amount of foreshortening, will depend on the angle of incidence to the film. The sample imaged in (B) was smaller than the incident beam cross section, and, thus, images of the entire crystal are produced.

3. X-RAY TOPOGRAPHY TECHNIQUES

In practice, there are many ways to create an X-ray topograph. Since each method has distinct advantages, a brief summary is given here of the classical XRT experiments. Among XRT techniques, section topography is the most fundamental. In section topography, diffraction from a restricted volume, or "section" is taken. The restricted volume is defined by X-ray entrance and exit slits. The section geometry is shown in Figure 4. It is performed using a monochromatic and spatially narrow ($\approx$ 10 µm) incident X-ray beam. Two diffracted beams are shown in Figure 4: the forward-diffracted O-beam, and the diffracted H-beam. The image from the crystal volume in which these beams interact (shown in Figure 4 as a triangular section) is recorded. In section topography, even the topograph of a perfect crystal displays fringes. Image interpretation usually involves modeling by means of the Takagi and Taupin equations [Takagi, 1962 and 1969; and Taupin, 1967]. These equations have the advantage that they can be used to describe general defects. The benefits of using section topography are that very small lattice strains can be observed because they result in a distortion of the observed fringes, defects can be located as a function of depth in the crystal [Lang, 1980], and one can distinguish between stacking faults and tilt boundaries [Capelle, *et al.,* 1982]. Finally, the analysis is quantitative because of the availability of computer simulation algorithms [Epelboin, 1999].
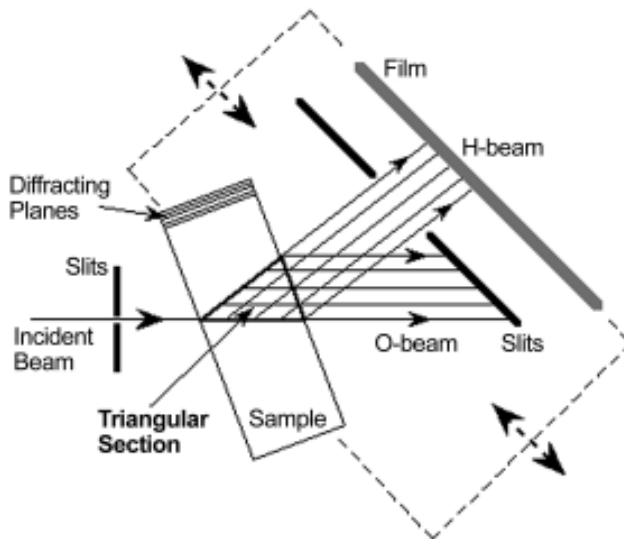
Figure 4. *The geometry for section topography. A narrow X-ray beam is incident on the sample crystal, and the transmitted diffraction image from a restricted region is recorded. The same geometry is used for projection topography where the sample and the film are scanned synchronously as indicated by the double arrows.*

In many applications, images from a restricted volume are not sufficient. The defect microstructure of the entire crystal specimen must be imaged. Starting from the section geometry, an integrated image over the entire specimen can be created if the specimen and the detector are translated synchronously in the pencil beam. (See Figure 4.) This method, invented by Lang, has been called "traverse" and also "projection" topography [Lang, 1959]. The traverse image is a superposition of the section images. This technique has been used to great advantage in X-ray laboratories, and many X-ray instrumentation manufacturers include Lang cameras as standard catalog items.
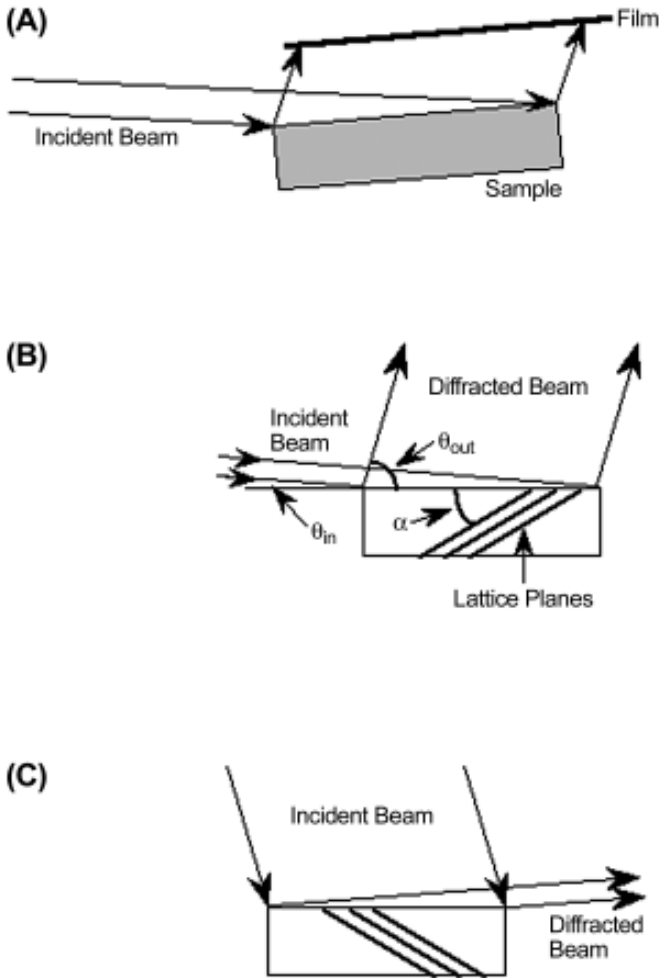
Figure 5. *The Berg–Barrett geometry is shown in (A). Asymmetric diffraction in the expansion or magnification geometry is illustrated in (B) and in the reduction or demagnification geometry in (C).*

Analogous to the transmission-diffraction geometry of Lang is the reflection-diffraction geometry of Berg–Barrett [Berg, 1931 and Barrett, 1945] topography, shown in Figure 5(A). In this geometry, the incident pencil beam reaches the crystal at grazing incidence, where it is diffracted by planes oblique to the sample surface (Figure 5(B)) under asymmetric diffraction conditions. Although asymmetric diffraction is mentioned here in the context of Berg–Barrett topography, diffraction can be asymmetric in transmission as well as in reflection. For either geometry, the asymmetry is specified by the parameter b ($b = 1/m$, where m is the magnification factor) where

$$-b = \frac{\sin (\theta_B + \alpha)}{\sin (\theta_B - \alpha)} \tag{2}$$

and the angle α is measured from the crystal plane to the crystal surface (for reflection) and to the crystal surface normal (for transmission). The advantage of asymmetric diffraction is that no rastering motions are needed to acquire a Berg–Barrett topograph of the entire crystal. The diffracted X-ray beam, however, is divergent due to defects in the crystal, so the imaging film or camera is placed as close as possible to the sample to retain spatial resolution. The Berg–Barrett method is another XRT technique that has been applied very successfully in X-ray laboratories.
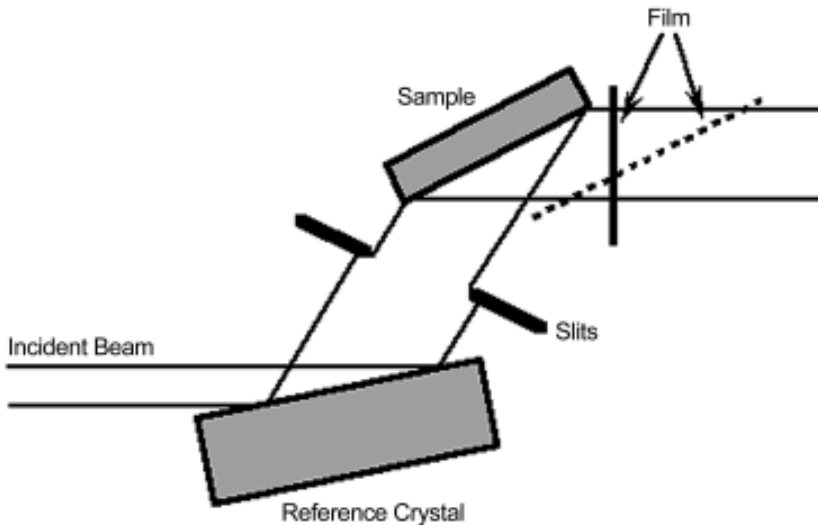
Figure 6. *Double crystal geometry for X-ray topography. The incident X-ray beam is "collimated" by diffraction from a high-quality reference crystal. The film is positioned perpendicular to the diffracted beam to maximize resolution or is placed parallel to the sample to provide a 1:1 image with no distortion or foreshortening.*

Improvements to the spatial resolution of Berg–Barrett topography, and a relaxation of its restrictive geometry, are possible by reflecting the incident X-ray beam from a high-quality reference crystal before using it to image defects in the sample crystal. The reference crystal serves to narrow the angular spread of the X-ray beam incident on the sample crystal. This is called the "double-crystal" geometry [Kohra, *et al*., 1962], shown in Figure 6, where the first crystal acts as a "collimator," and the second crystal is the sample. This technique has been used successfully in the laboratory, but the exposure times to produce a topograph may be measured in hours or even days. The double-crystal geometry became much more useful with the advent of intense synchrotron X-ray sources, where the exposure times are reduced by many orders of magnitude.

4. IMAGE CONTRAST IN X-RAY TOPOGRAPHY

Topographic contrast, *i.e.*, the point-to-point variation in diffracted intensity, is generally understood in terms of two mechanisms: orientation contrast and extinction contrast [Petroff, 1984]. Orientation contrast can be explained by the simple application of Bragg's law. Extinction contrast, however, is described by means of kinematical [Zachariasen, 1945] and the dynamical [Batterman and Cole, 1964; Zachariasen, 1945] theories of X-ray diffraction. Although dynamical theory accounts for most of the image contrast in XRT, a detailed description of dynamical theory is outside the scope of this guide. Instead, the important concepts derived from dynamical theory are discussed as they apply to an analysis of XRT data. The reader may wish to consult some of the many available resources [Authier, 1970; Kato, 1996; Lang, 1973; Hart, 1980; Authier, *et al.*, 1996; Bowen and Tanner, 1998] for a more complete description of dynamical theory with reference to XRT.

First, however, orientation contrast is described. As the name implies, orientation contrast arises when parts of the sample are oriented such that they do not satisfy the Bragg condition. To understand orientation contrast, one can imagine a monochromatic X-ray beam incident on a sample composed of areas that are crystallographically misoriented (*e.g.*, there exists subgrain structure or strain) compared to the rest of the crystal. If these areas are misoriented sufficiently such that they are outside the reflection range (rocking curve) of the crystal, they cannot satisfy the Bragg condition and therefore they will not diffract. For areas that are less misoriented, the diffracted intensity can take on any value from negligible to nearly the intensity diffracted by the surrounding crystal. To illustrate orientation contrast, an early example from Lang [1970] is offered here. Consider a perfect crystal containing a region (A) that is misoriented with respect to the rest of the crystal but has the identical lattice spacing, Figure 7(a). For monochromatic incident X-rays, and the sample oriented in the Bragg reflection geometry to diffract from the crystal matrix, the misoriented region will not satisfy the diffraction condition, and, therefore, the image arising from this region will appear white against the matrix image, Figure 7(b).

A qualitative, general understanding of extinction contrast in the Bragg reflection geometry is available from a continuation of the above example. Another region (B), Figure 7(c), is imperfect compared to the matrix but has the same orientation, *e.g.*, the region in the vicinity of a dislocation. In this case, the diffracted intensity is determined by the local scattering power. The scattering power from diffraction by perfect and imperfect crystals is different. The FWHM (rocking curve angular width) of a perfect crystal is very narrow, the peak reflectivity is close to 100%, and its scattering power (its integrated reflectivity) is proportional to the structure amplitude of the

Bragg reflection, $|F|$ [Cullity, 1967]. By comparison, the FWHM of an imperfect crystal is broad, the peak reflectivity is much less than 100%, but the integrated reflectivity is proportional to $|F|^2$. Thus, the diffracted X-ray intensity from imperfect regions of a crystal is much greater than that from the surrounding perfect crystal matrix (Figure 7(d)). An example of increased intensity from deformed regions surrounding dislocations is shown in a reflection topograph from a sapphire crystal in Figure 8. The upper panel in this figure is a $(0\,0\,0\,12)$ symmetric reflection topograph, and the lower panel is an enlargement of the lower right portion of the image. Dislocations are seen as dark lines. Other visible features are described in the figure caption.

Returning to X-ray contrast in Bragg reflection topography, the fundamental difference between the kinematical and the dynamical theories of X-ray diffraction is that the scattering at each atomic site is independent when kinematical diffraction takes place, and the incident and the diffracted waves

(a) (b)

(c) (d)
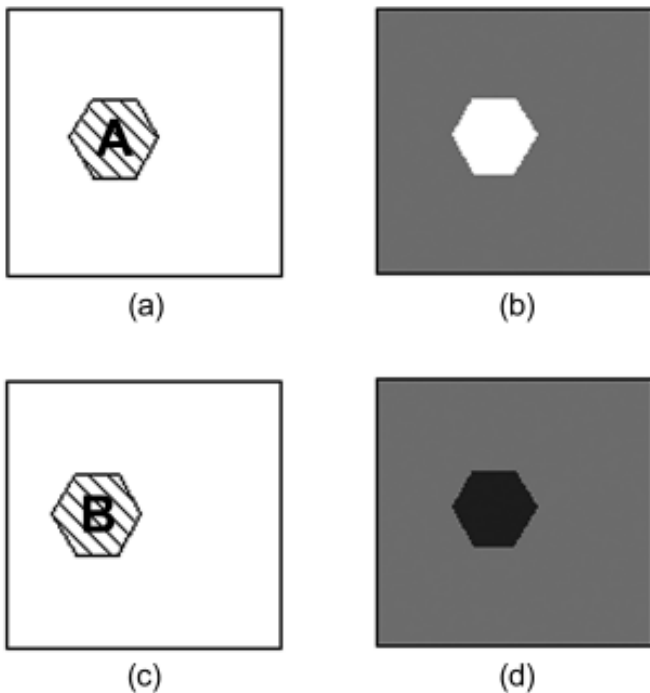
Figure 7. *A perfect crystal matrix is shown in (a) containing a region, A, misoriented by more than the rocking curve width of the matrix. A monochromatic X-ray topograph from this crystal is shown schematically in (b), where region A does not satisfy the diffraction condition. If another region, B, is imperfect, but has the same orientation as the matrix as shown in (c), a reflection X-ray topograph will show more intensity from region B than from the perfect matrix as indicated in (d).*
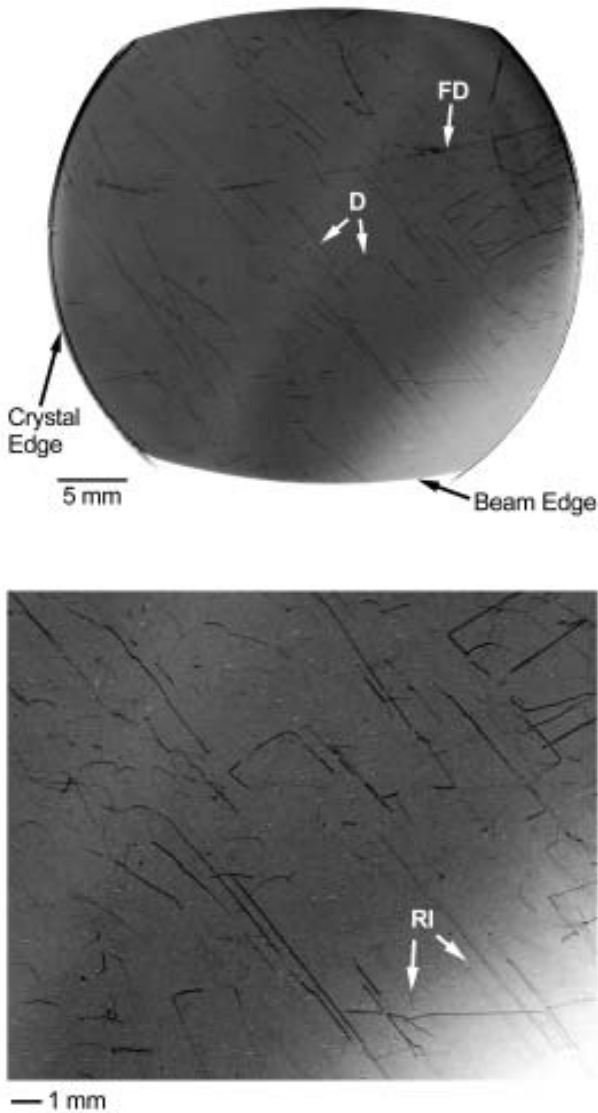
Figure 8. *Symmetric reflection (0 0 0 12) topograph from a sapphire crystal showing dark dislocation images (D). The incident beam was larger than the sample in the horizontal direction but smaller than the sample in the vertical direction. Therefore the kinematic intensity at the edges of the sample is seen on the sides. The beam edge defines the image at the top and bottom. The reduced intensity in the lower right hand corner is due to a slight tilt of the sample diffracting planes with respect to the monochromator diffracting planes. The lower panel is a magnified view of the lower right portion of the upper panel. The large dark feature (FD) is damage in the film emulsion. The light grey images (RI) are radiographic images from defects on the beryllium window separating the experimental hutch from the monochromator chamber.*

within the crystal interact when dynamical diffraction takes place. Dynamical diffraction is generally seen in thick crystals of good quality, *i.e.*, with rather low defect density. In dynamical Bragg reflection, the wave fields diffract back toward the surface (rather than continue into the sample) where they add to the reflected beam at the surface. As a result, the x-rays penetrate much less than would be the case if there were only true (photoelectric) absorption. This effect is called "primary extinction." Thus, for primary extinction, the scattering amplitudes are added before the total intensity is calculated. On the other hand, kinematical diffraction is generally seen when the crystal is imperfect. Here the X-rays penetrate further than they would if the crystal were perfect, but still less than for true absorption. This effect is called "secondary extinction." When secondary extinction takes place, the total intensity is calculated by adding the scattering intensities directly. Since there is increased diffracted intensity from imperfect regions in a crystal arising as a result of a reduction in primary extinction, the term "extinction contrast" [Newkirk, 1958] came into use.

In transmission (Laue) diffraction by thick crystals of good quality, dynamical theory shows that X-ray energy is transferred between the forward-diffracted O-beam and the transmitted-diffracted H-beam. As the waves traverse through the crystal, they can decouple at defect sites and create new wave fields, thereby changing the appearance of the diffraction image. Thus, defects are observed as "disruption images" and are seen in topographs as a *reduction* in intensity. An example of this is shown in Figure 9, which is a transmission topograph of the same sapphire crystal shown in a reflection topograph in Figure 8. The lower image in Figure 9 is a magnified view of a portion of the upper image. Dislocations in this transmission topograph are seen as white features. Dislocations near the exit surface (such as D1) are sharply defined, while those further from the exit surface (such as D2) appear fuzzy. Interestingly enough, some secondary extinction contrast (black contrast) can be seen for crystal defects very close to the exit surface of the X-ray beams, where dynamical diffraction reverts to kinematical.

As indicated above, kinematical theory typically accounts for diffraction contrast in images from thin crystals and very distorted crystals, whereas dynamical theory accounts for diffraction contrast in images from thick, good quality crystals. Here, the linear absorption coefficient, μ_0, associated with the photoelectric effect is used to define "thick" and "thin." If, $\mu_0 t < 1$, where t is the crystal thickness, the crystal is considered "thin" and the kinematical theory is usually (but not always) operative; if, $1 < \mu_0 t < 10$, the thickness is intermediate, and the dynamical theory may or may not be dominant; if $\mu_0 t > 10$, the crystal is "thick" and the dynamical theory is operative.
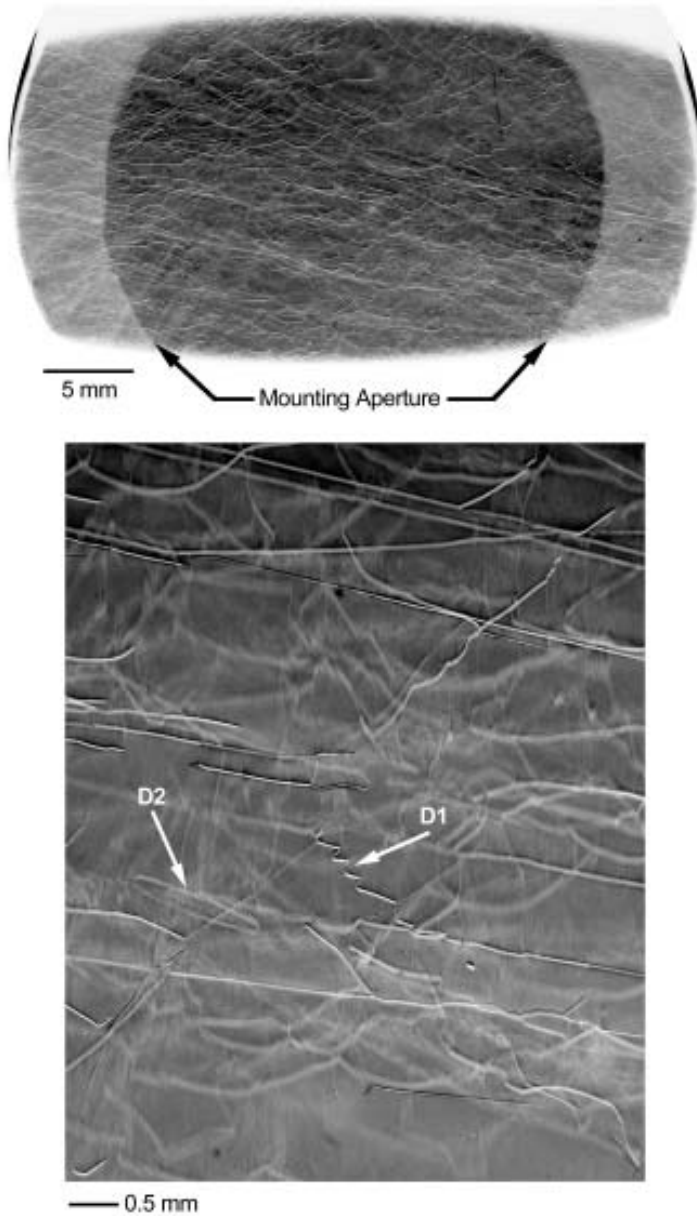
Figure 9. *Symmetric transmission image from the same sapphire crystal shown in Figure 8. This crystal is 2 mm thick, and the photoelectric absorption $\mu_0 t = 25$ at 8 keV, so the image is formed by anomalous transmission. The dislocation images are white on a dark background. The sample was mounted on a plastic ring with a circular aperture, and the reduced intensity, due to absorption by the plastic, is seen as the lighter regions on the left and right sides of the image. The lower panel is a magnified view of a region shown in the upper panel. Dislocations near the exit surface (D1) are sharper than those closer to the entrance surface (D2).*

The dynamical theory requires the solution of Maxwell's equations inside the crystal consistent with the periodicity of the crystalline lattice and with continuity of the electric field across the crystal/vacuum boundary. The interaction of the diffracted wave fields within the crystal produces a number of important effects that are observed in topographs. First, as mentioned above, when a crystal is oriented so that it diffracts X-rays, the absorption is very different from photoelectric absorption. In this case, one calculates absorption from the imaginary part of the wave fields, which leads to two important results: the diffraction "extinction length" and the existence of "anomalous transmission." The diffraction extinction length is analogous to the optical 1/e rule in photoelectric absorption, and is given by [Authier, 1996]:

$$\xi = \pi V / \lambda r_e |F|,$$

(3)

where r_e is the classical radius of the electron and V is the unit cell volume. The extinction length is a measure of the depth of X-ray penetration when a Bragg condition is satisfied, and it sets the minimum thickness for extinction contrast to be observed in images. The size of defect images also scales with the extinction length, as shown below.
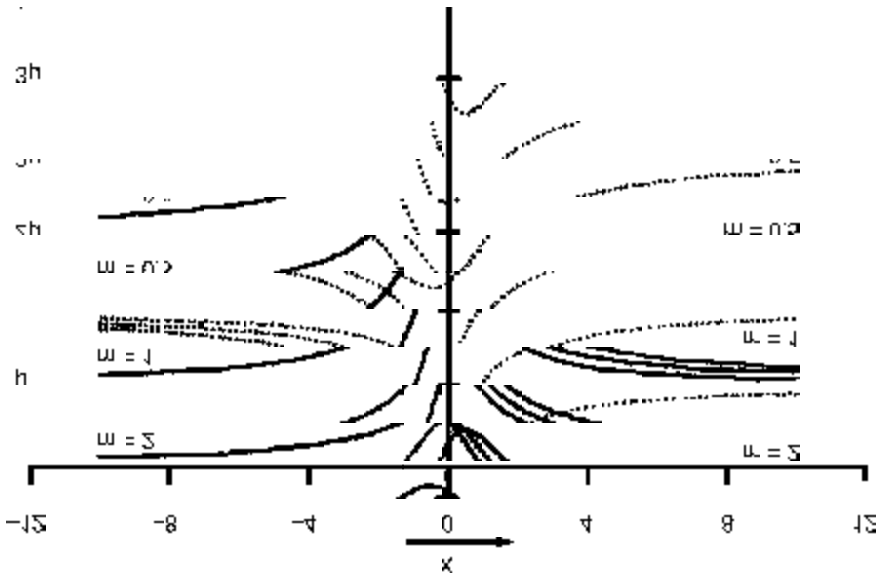
Figure 10. The effective absorption coefficient for symmetric and asymmetric Laue diffraction as a function of deviation from the exact Bragg angle at X = 0. The dashed lines are for Branch 1, and the solid lines are for Branch 2. Far from the Bragg angle, the effective absorption coefficient approaches the photoelectric absorption coefficient.

Another result of dynamical diffraction is anomalous transmission or the "Borrmann effect" [Borrmann, 1941 and 1959; Borrmann, *et al.*, 1958]. The solutions to Maxwell's equations inside the crystal are expressed as a hyperbloid of revolution around the Laue point called the Dispersion Surface. The dispersion surface has two branches, Branch 1 and Branch 2, which describe wavefields that are π out of phase with respect to each other. X-ray transmission topographs show a strong reduction in the effective absorption of X-rays for Branch 2. The reduction is sufficiently large that a diffracted beam can be transmitted through a high quality crystal with a photoelectric absorption as high as $\mu_0 t \approx 30-50$. In an illustrative example, Batterman and Cole [1964] calculated the absorption of wave fields at the center of the Bragg diffraction range. For the 220 reflection in a 1-mm-thick Ge crystal, the ordinary absorption $\mu_0 t = 38$ for 8 keV photons. The effective absorption is 74 for diffracted X-rays in Branch 1 and 1.9 for diffracted X-rays in Branch 2. Thus, the crystal is rather transparent to diffracted X-rays of Branch 2. This weak absorption is observed for the wave field that has the nodes of its stationary waves located between the atomic planes. The effective absorption coefficients for Branch 2 and Branch 1, as a function of diffraction angle, are shown in Figure 10 for symmetric diffraction (m = 1) and for two cases of asymmetric diffraction (see Equation 2). Far from the Bragg condition,
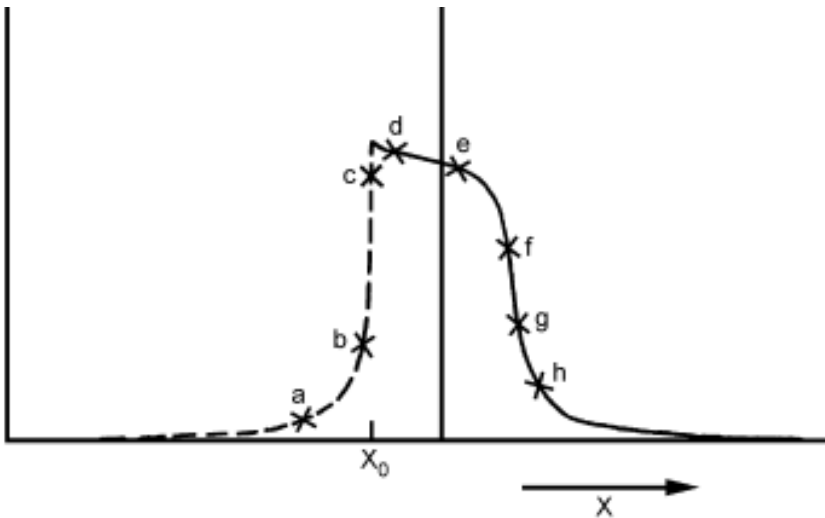
Figure 11. The symmetric Bragg rocking curve from a crystal with finite absorption. The solid line is the contribution from Branch 1, and the dashed line is the contribution from Branch 2. The labeled positions on the rocking curve are the points where the topographs shown in Figure 12 were recorded.

the effective absorption for the symmetric case is the linear photoelectric absorption coefficient. Near Bragg, *i.e.*, near X = 0, the absorption dips for Branch 2 and peaks for Branch 1. Results for asymmetric diffraction are more complicated, but similar [Kuriyama and Cohen, 1982].

When the scattering amplitude is calculated for dynamical Bragg reflection, both branches contribute to the X-ray intensity in the crystal rocking curve. Branch 1 is shown by a solid line and Branch 2 by a dashed line in the rocking curve shown in Figure 11. Crossing over from one branch to the other, white and black contrast is interchanged [Kuriyama and Long, 1984]. At each angular position along the rocking curve, a distinct topographic image can be recorded. In Figure 12, (0 0 6) symmetric reflection topographs of a bismuth silicon oxide crystal [Steiner, *et al.*, 1988], taken at the positions indicated in Figure 11, are shown. The best contrast is seen in images taken on the rapidly changing wings of the rocking curve, where striations created during crystal growth are seen. The contrast in images (b) and (c) is inverted from that of images (f) and (g). Images (d) and (e), taken near the peak of the rocking curve, show mostly surface scratches because here the beams are confined to the near surface region of the crystal. Images taken far out on the wings of the curve are referred to as "weak beam" images; there the diffracted beam penetrates into the sample crystal, and sensitivity to bulk crystal structure is enhanced.

An additional source of contrast, Fresnel imaging due to phase contrast, is often observed at synchrotron X-ray sources because of spatial coherence in the incident beam. An image may be formed by a low-absorbing sample or indeed by any object in the X-ray path. A phase image is created by local variations in the optical path of the X-rays due to phase variations across the beam related to microstructures within the object. These images indicate, for example, the presence of pores, internal boundaries, thickness variations, etc., which are made visible depending on the object-to-detector distance. Now recognized as an imaging technique in its own right, phase contrast radiography [Cloetens, *et al.*, 1999] is usually a source of unwanted image contrast for XRT.

One final topic regarding image formation in X-ray topography is related to the frequently asked question: how do atomic-scale defects such as dislocations produce micrometer-scale images in X-ray topographs? The answer can be found by comparing the distorted regions around the dislocations to the rocking curve range for the defect-free regions of a crystal. The following discussion follows along the lines of examples in Lang [1973], Tanner [1996], and Bowen and Tanner [1998]. The rocking curve width for symmetrical Bragg diffraction in the absence of absorption is

$$\Delta\theta = 2/g\xi. \tag{4}$$
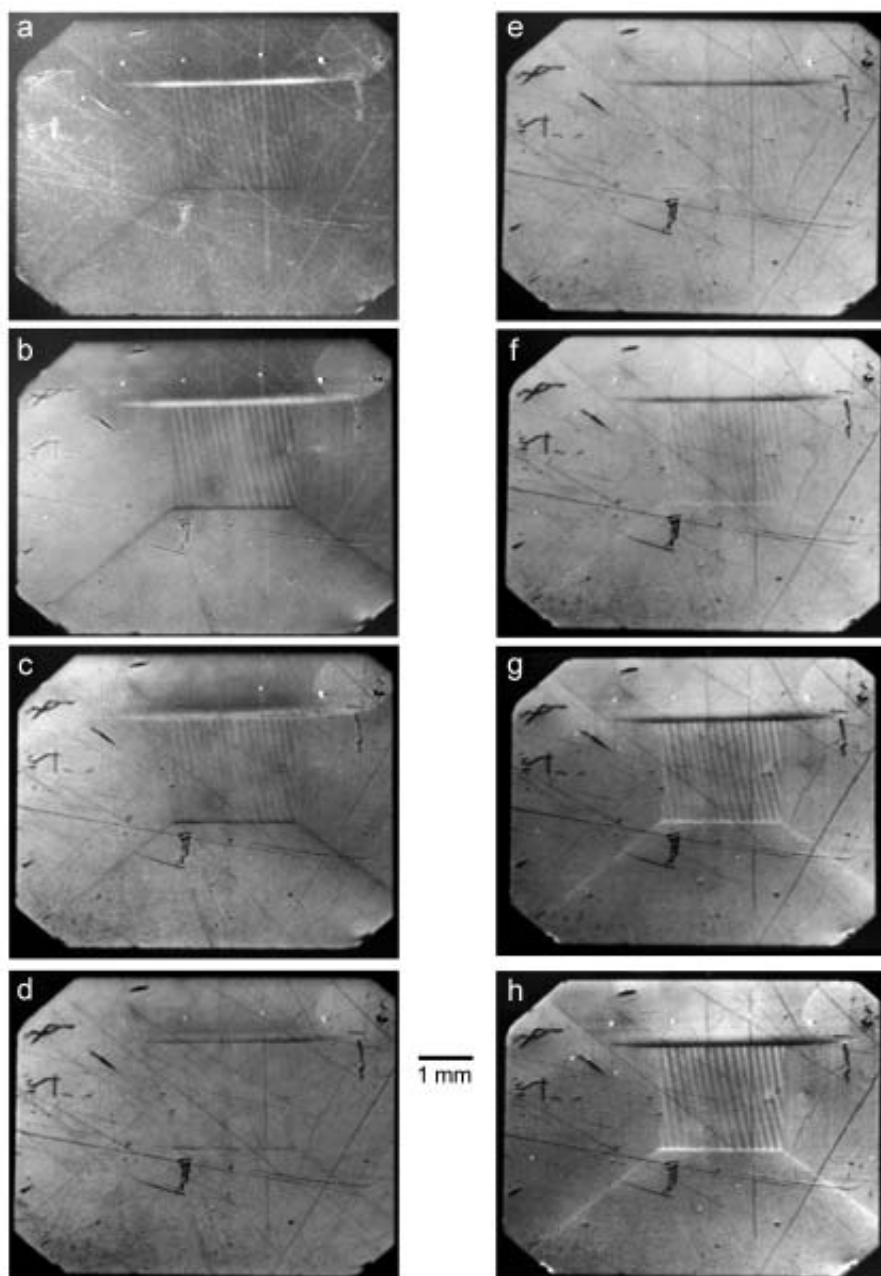
Figure 12. *Symmetric (0 0 6) surface reflection topographs from a bismuth silicon oxide crystal recorded at the positions indicated on the rocking curve of Figure 11. The contrast reverses between the two branches. These images were recorded on a video camera, rather than X-ray film, and, therefore, they have the opposite contrast from all the other images shown above. Here, increased diffracted intensity appears light, and decreased intensity appears dark.*

In a simple model of a dislocation, there is a distorted region surrounding the dislocation which falls off as the inverse of the distance from the dislocation core. For a screw dislocation perpendicular to the diffracting planes, the distortion can be described as

$$\Delta\omega = B/2\pi R \tag{5}$$

where B is the Burgers vector and R is the distance from the dislocation core. The distorted region defines the part of the crystal around the defect that behaves as an imperfect crystal, with the consequent increased diffracted intensity in its image. The size of the region depends on the angular range of the perfect crystal rocking curve. When the distortion exceeds the diffraction rocking curve width, the intensity distribution is described by imperfect crystal (kinematical) theory. Therefore, the effective size, W, of the dislocation is twice the maximum radius as determined from $B/2\pi R \approx 2/g\xi$ or:

$$W = 2R \approx Bg\xi/2\pi. \tag{6}$$

The general result for any arbitrary dislocation line direction is [Tanner, 1996]:

$$W \approx \mathbf{B} \bullet \mathbf{g}\, \xi/2\pi \qquad \text{for screw dislocations, and}$$

$$W \approx 0.88\, \mathbf{B} \bullet \mathbf{g}\, \xi/2\pi \quad \text{for edge dislocations.} \tag{7}$$

As an example, consider a (200) diffraction from an aluminum single crystal, where primary slip has occurred along {111} planes. With an 8 keV incident X-ray beam, dislocation images are expected to be about 4.7 μm wide. The large widths of these images, compared to those from transmission electron microscopy for example, are a direct consequence of the high strain sensitivity of XRT. The width of XRT images also limit the defect density for which individual dislocations can be resolved to approximately $10^4/cm^2$. Hence, a "good quality" crystal from the perspective of x-ray topography has a defect density $\leq 10^4/cm^2$. Another result of Equation 6 is that the size of the defect image is a function of the structure factor as well as the incident X-ray energy. Since the extinction length depends on both the X-ray wavelength (energy) and the structure factor (Equation 3), it becomes evident that the image width increases as the X-ray energy is increased or as the structure factor is decreased.

5. PRACTICAL ASPECTS OF THE METHOD

Monochromatic X-ray topography at a synchrotron facility requires the introduction of a monochromator into the X-ray optical path. The monochromator serves to select a particular energy or wavelength from the incident beam. Once past the monochromator, the power in the X-ray beam is significantly reduced and the probability of radiation damage to the sample crystal is lessened. In addition to wavelength, λ, selection, the monochromator can be used to improve the angular collimation so that it is very narrow and the plane wave approximation is applicable. Asymmetrical diffraction in the monochromator can be used to increase (Figure 5(B)) or reduce (Figure 5(C)) the physical size of the X-ray beam on the sample so that, in the first case, large crystals can be imaged in a single exposure, or, in the second case, the defect microstructure of small, weakly diffracting crystals can be imaged.

There are a variety of monochromators currently in use at synchrotron radiation facilities — single crystal and multiple crystal designs. The important point is that the X-ray optics can be used to prepare the X-ray beam so that the optimal spatial and angular resolutions are achieved and the information content of the topographic image is maximized. Since only one topograph is created at a time, that image can be recorded with the detector very close to the sample, thereby maximizing resolution.
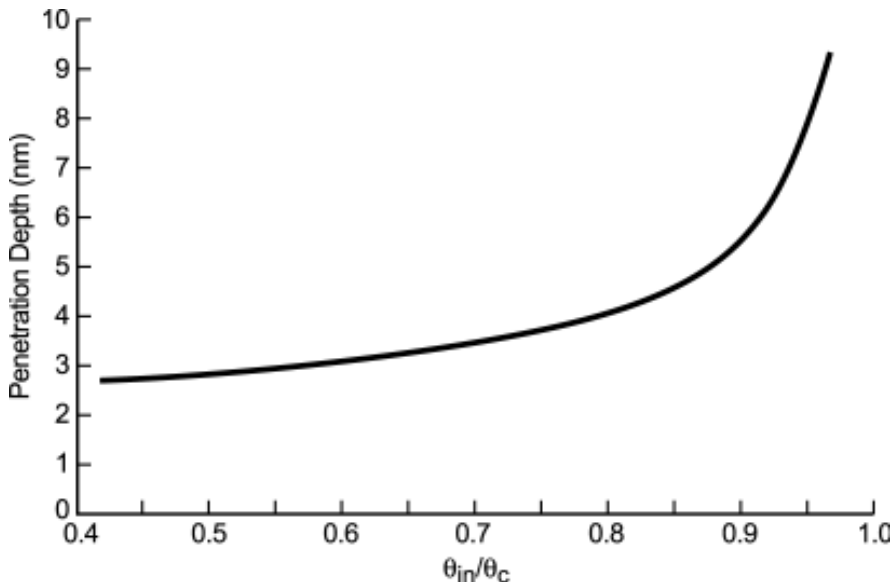
Figure 13. *The depth of penetration as a function of incidence angle just below the critical angle, θ_C, for total external reflection.*

Surfaces and thin films, as well as bulk microstructures, can be probed with monochromatic X-ray topography. For studies of surfaces, two methods are available. With symmetric surface reflection, the depth of penetration decreases the closer the diffraction image is taken to the top of the crystal rocking curve. As noted earlier, the images in Figure 12(d) and 12(e) near the top of the rocking curve display the sample's surface scratches, while the images in Figure 12(a) and 12(h) display more of the bulk growth-striation microstructure. The depth of X-ray penetration varies by almost an order of magnitude as a function of the Bragg angle. The other approach is a grazing-angle asymmetric Bragg geometry [Imamov, *et al*., 1989; Novikov, *et al*., 1995]. In this case, we are combining asymmetric diffraction with total external reflection in the same experiment. One prepares a grazing incidence condition by selecting an asymmetric surface diffraction. Then the incident photon energy is selected to establish a diffraction condition such that the incident angle is just above or just below the critical angle for total external reflection of the X-ray beam. Below the critical angle, the penetration into the sample can be less than 3 nm, see Figure 13, and the depth of penetration changes significantly with small adjustments of the incident energy around the critical angle.

6. SAMPLE GEOMETRY FOR DIFFRACTION IMAGING

The geometry of prospective XRT sample crystals generally conforms to their intended application in technology, rather than to optimal XRT standards. Nevertheless, it is very useful to understand what the parameters of an ideal XRT sample are. There are two classes of experiments, depending on the information that is required: surface microstructure or bulk microstructure. The ideal sample for imaging the surface microstructure is described first.

An XRT sample crystal is usually in the form of a flat plate with a well-defined surface of known crystallographic orientation. A surface reflection topograph can be recorded under three different geometric
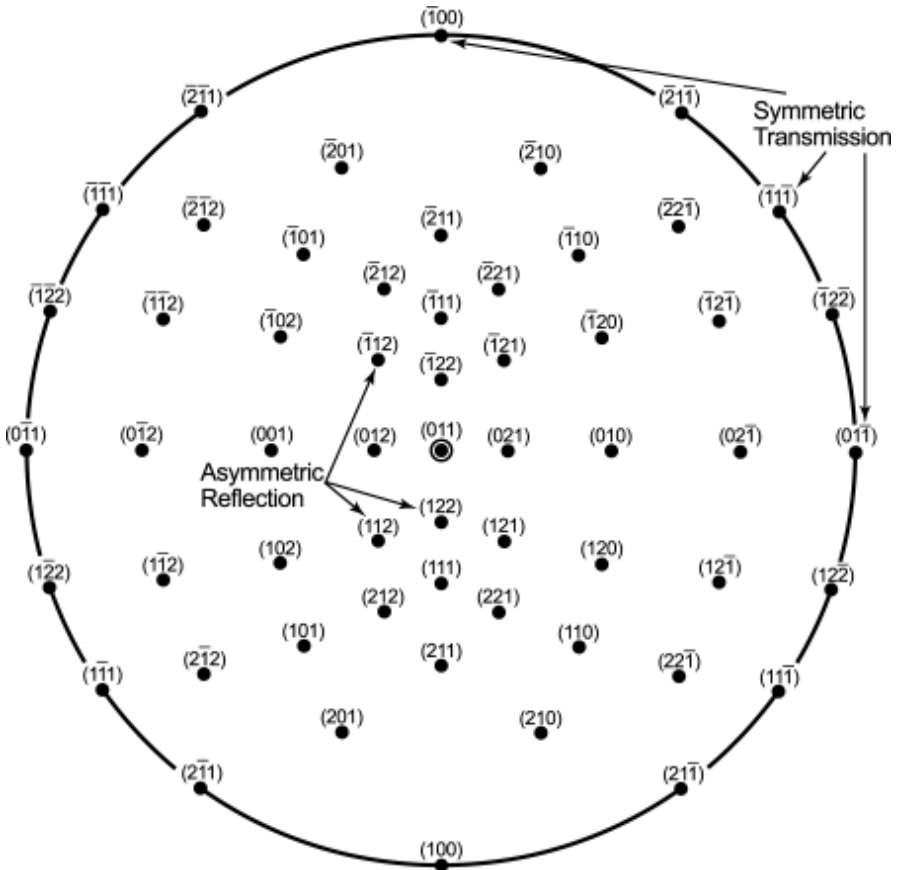
Figure 14. *A (110) stereographic projection for a cubic crystal. Planes near the center, as indicated, are candidates for asymmetric reflection while those near the circumference are candidates for asymmetric transmission. Planes on the circumference provide symmetric transmission images.*

23

conditions: symmetric diffraction, asymmetric diffraction, and grazing-incidence asymmetric diffraction. With a monochromatic incident beam, only one of these conditions can be established at a time. The availability of diffraction planes for imaging is determined by the crystallographic orientation of the sample relative to its surface, the diffractions which are allowed (*i.e.*, the structure factor), and the photon energy available from the monochromator. Most monochromatic XRT facilities can provide X-rays in the range from 5 keV to 25 keV.

The easiest image to obtain is from symmetric surface diffraction. In this case, the diffracting planes lie parallel to the sample surface, and the diffraction vector is along the surface normal. The symmetric reflection image yields information on defect microstructure that has a projection perpendicular to the crystal surface. The image is not sensitive, however, to defects parallel to the surface since, in that case, $g \cdot u = 0$.

Asymmetric diffraction is used to image microstructure parallel to the surface. The asymmetric diffractions that are available depend on the surface orientation. These can be found from a stereographic projection as in Figure 14. Crystallographic planes with normals close to the surface normal are candidates for asymmetric surface diffraction images. On the stereographic projection, these candidates are close to the center. Of course, the inclination angle of the selected diffraction planes with respect to the crystal surface must be smaller than the Bragg angle for the incident X-ray energy. For a silicon (110) surface, there are {211} planes inclined 30° from the surface and the Bragg angle for a (422) diffraction is about 44° for 8 keV incident photons. Therefore, the (422) asymmetric diffraction is possible with $\theta_{in} = 14°$. However, for a silicon (111) surface, there are {311} planes $\approx 29.5°$ away from the surface. For an 8 keV incident beam, the Bragg angle for the {311} planes is about 28°, so asymmetric (311) diffractions are not possible. If a (311) diffraction image is required, lower energy incident photons will bring the Bragg angle for (311) diffraction into the accessible range.

The third reflection geometry is the grazing-incidence asymmetric diffraction geometry, which is an extreme form of the asymmetric geometry just described. For monochromatic radiation, the diffracting plane and the incident photon energy are chosen so that the X-ray angle of incidence is extremely small. Then the depth of X-ray penetration is also very small. (See Figure 13.) Also, the microstructure parallel to the surface will be imaged because it has the largest projection in the direction of the diffraction vector for that diffraction. Further, the specific depth of penetration can be selected by means of the incidence angle. An example of the depth sensitivity of grazing-incidence asymmetric diffraction imaging is shown in Figure 15. The depth of penetration in the left panel (above the critical angle) is much greater than that

E = 9.60 keV   E = 9.70 keV

1 cm
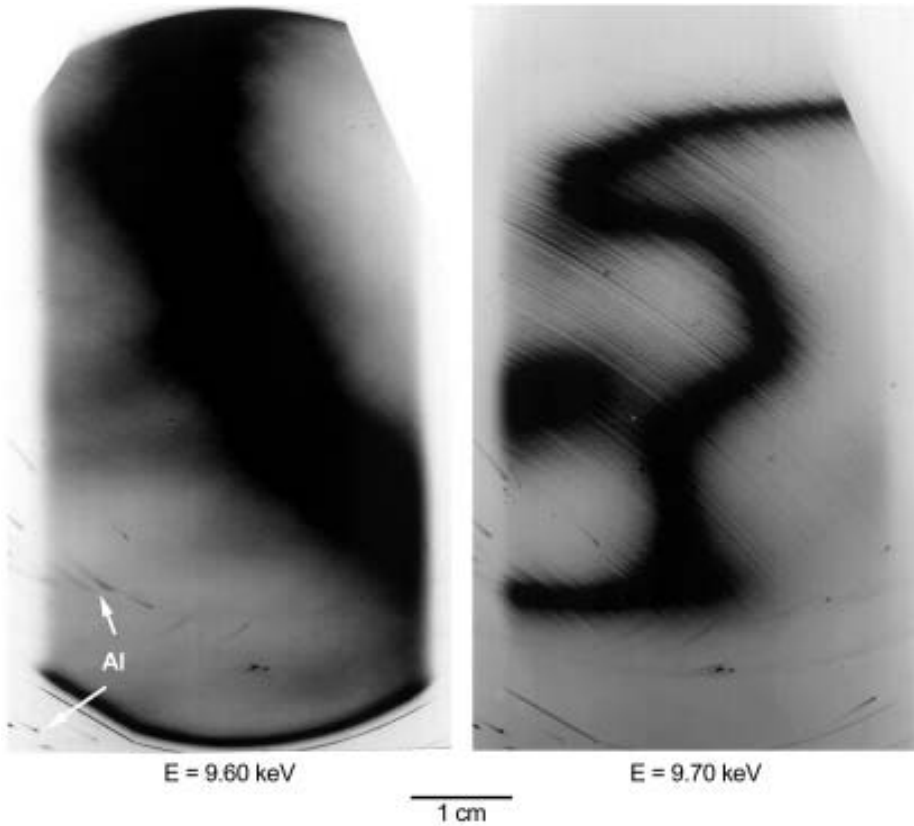
Figure 15. *An example of the depth sensitivity of X-ray images above and below the critical angle for total reflection. This is a* (11$\bar{2}$9) *asymmetric diffraction from a sapphire crystal. The microstructure that can be seen above the critical angle, the left image, indicates that the sample is strained. Below the critical angle, in the image on the right where the near surface region is imaged, the sample exhibits much more strain and residual polishing damage. The incident beam was slightly larger than the crystal and impinged on the aluminum mounting ring. This produced diffraction images (Al) from individual grains in the polycrystalline aluminum.*

in the right panel (below the critical angle). While both show strain patterns, the right panel shows that the strain closer to the surface is greater, and there is residual surface damage from surface processing.

Next, samples for experiments to image the bulk microstructure are described. The transmission geometry is used in this case, where it also is divided into two cases: symmetric diffraction imaging and asymmetric diffraction imaging. The candidate planes for transmission diffraction imaging lie in an annulus near the circumference of the stereographic projection such as in Figure 14. Diffraction

from planes indicated on the circumference is symmetric, and diffraction from all others is asymmetric. For a cubic crystal, a (110) surface is particularly useful in that symmetric transmission diffraction from {001}, {110} and {111} planes are available. Returning to the example of dislocation structures, it is often necessary to describe the dislocation images in X-ray topographs in terms of the dislocation type (edge or screw) and their interactions. Both types of dislocations are lines, but screw dislocations have no X-ray contrast if $\mathbf{g} \cdot \mathbf{B} = 0$ and edge dislocations have no contrast if $\mathbf{g} \cdot (\mathbf{B} \times \mathbf{l}) = 0$, where $\mathbf{B}$ is the Burgers vector and $\mathbf{l}$ is the dislocation line direction. Thus, the dislocations in XRT images can be sorted according to type by finding where they are invisible. With a (110) sample surface, symmetric transmission images can be taken in each of the principle directions.

If the sample thickness is such that $\mu t \geq 10$, image interpretation is straightforward. For a silicon crystal and 8 keV incident photons, μ/ρ, the mass absorption coefficient, is 61.8 cm^2/g and the density is 2.33 g/cm^3. To achieve $\mu t \geq 10$, the sample should be at least 0.7 mm thick. If the thickness cannot be changed, the incident photon energy can be changed to bring the experimental conditions closer to $\mu t \geq 10$. For a silicon crystal, for example, the mass absorption coefficient changes by a factor of 33 between 6 keV and 20 keV. However, the defect image width also increases with increasing X-ray photon energy.

7. SAMPLE PREPARATION

Sample preparation is a key element of successful XRT. To achieve topographic images representative of the defect microstructure to be studied, great care must be taken to avoid introducing damage into the sample during sample preparation and mounting. This section is divided into two parts: the preparation of sample surfaces, and the handling and mounting of samples. A resource on this subject is Chapter 13 in Tanner and Bowen [1980].
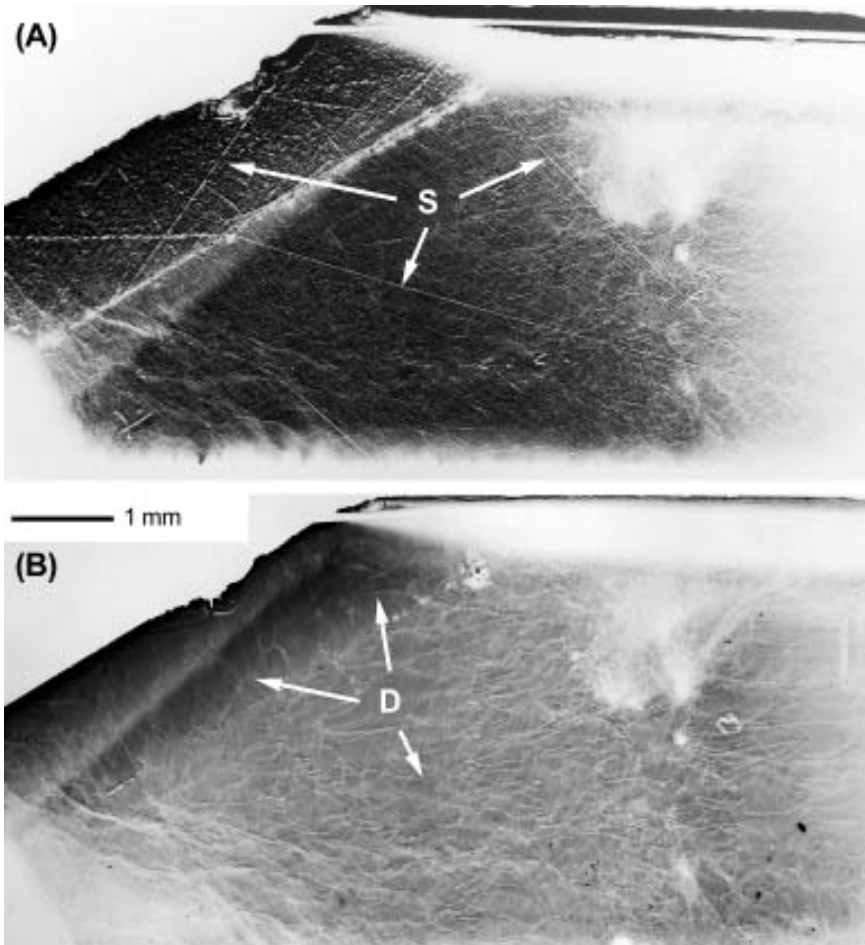
Figure 16. *Surface preparation can have a profound effect on topographic images. The ZnSe crystal shown in (A) was prepared using a standard abrasive-polishing procedure. This image is dominated by surface scratches (S), and the underlying bulk microstructure cannot be seen. After the crystal was etched to remove residual damage, the image shown in (B) allows the observation of the bulk dislocation (D) structure.*

The goal of sample preparation is to obtain a flat, smooth, damage-free surface that will not contain features that mask the bulk or surface microstructure of interest. The degree to which surface damage can interfere with the required data depends on the geometry of the measurement. Asymmetric surface diffraction topographs are extremely sensitive to surface structure, and thus an improperly prepared surface, if present, will dominate the data. The transmission geometry, by comparison, can be less sensitive to surface damage depending on the severity of the damage and whether the damage is on the X-ray beam entrance or exit surface. Minor damage on the entrance surface in transmission geometry may cause little obscuration of data. The main effect is that the overall beam intensity is lowered. The quality of the exit surface, however, is critical for transmission imaging. Even minor damage on the exit surface will dominate the transmission image, and, as with reflection images, may obscure the microstructure of interest.

In general, a crystal sample should be polished and etched to prepare as clean a surface as practical. A note of caution: an optically-smooth polished surface is not always optimal. In the example shown in Figure 16, a ZnSe crystal was prepared for XRT by polishing to a mirror finish. This process left considerable residual scratches, as seen in Figure 16 (A). After this crystal was etched to remove the polishing damage, the bulk dislocation structure became visible in the transmission topograph, Figure 16 (B).
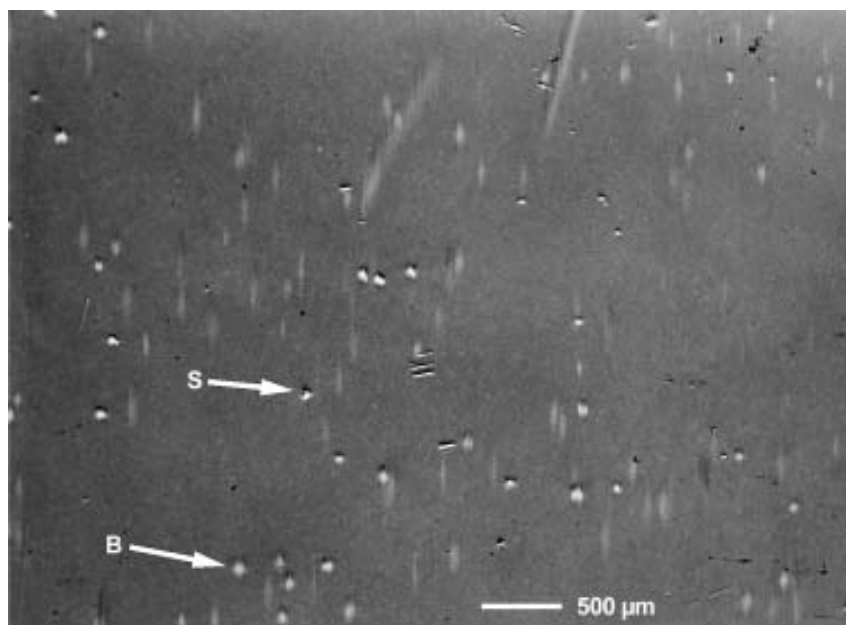
Figure 17. *A silicon crystal with surface damage. The damage on the entrance surface (B) appears blurry whereas damage on the exit surface (S) appears sharp.*

The difference between the appearance of entrance surface damage and exit surface damage in the transmission topography geometry is shown in Figure 17. This silicon wafer under investigation has damage on both surfaces. The entrance surface damage appears diffused or blurred, whereas the exit surface damage appears crisp.

The guiding principle when preparing and handling a crystal for XRT is to perturb the crystal as little as possible. While it may be straightforward to mount a crystal rigidly to a support, it is not particularly straightforward to do this without introducing strain. XRT is sensitive to orientational variations as small as 5 µrad, which means for a 1 cm diameter sample, a radius of curvature as slight as 1000 meters can reduce the diffracted image area. Therefore, only the most gentle (but secure) mounting methods can be used. Furthermore, for the highest quality images, the sample must also be stationary in the X-ray beam since small vibrations can cause the sample to flutter in the beam and cause the image to become blurred. For some orientations, the sample is likely to be rotated almost upside down, so the mount must support the full weight of the crystal. For transmission images, both surfaces should be free of mounting materials over as large an area as possible.

The requirement of a strain-free yet rigid mounting is a non-trivial problem. No single method works for all samples. For many applications, a trial and error process is needed to find the right mounting. This is an opportunity to be creative. Some of the successful mounting products that have served over the years include: a glue made of styrene packing material (peanuts) dissolved in zylene, a rubber-based double-stick adhesive tape, a variety of putties and clays, crystal mount, "blue" tack, surface tension mounting with viscous fluids, and diffusion bonding of a metal crystal to a high-purity backing plate of the same material [Black and Burdette, 1986]. To avoid obscuring or shadowing the incident or the diffracted beam, the sample mount should also have a low profile. In general, samples will be mounted to a goniometer head of some type. Typical goniometer heads are those from Huber* and Rigaku.*

Given a sample or samples with the appropriate orientation and thickness, one is ready to record images. A prime consideration is to get the recording medium as close as possible to the sample to maximize spatial resolution. The image can be captured digitally from a real time video camera, acquired digitally from an integrating CCD camera, or recorded on high-resolution X-ray film. To find and optimize a particular diffraction condition, it is extremely useful to have a real-time video camera to observe the diffracted image as the Bragg condition is changed. Cameras are available with a pixel size from 9 µm with an image area of 58 mm^2 up to an image area of 6348 mm^2 with a pixel size just under 150 µm. While electronic imaging detectors are extremely useful, the best resolution is still obtained by photographic means.

5 mm
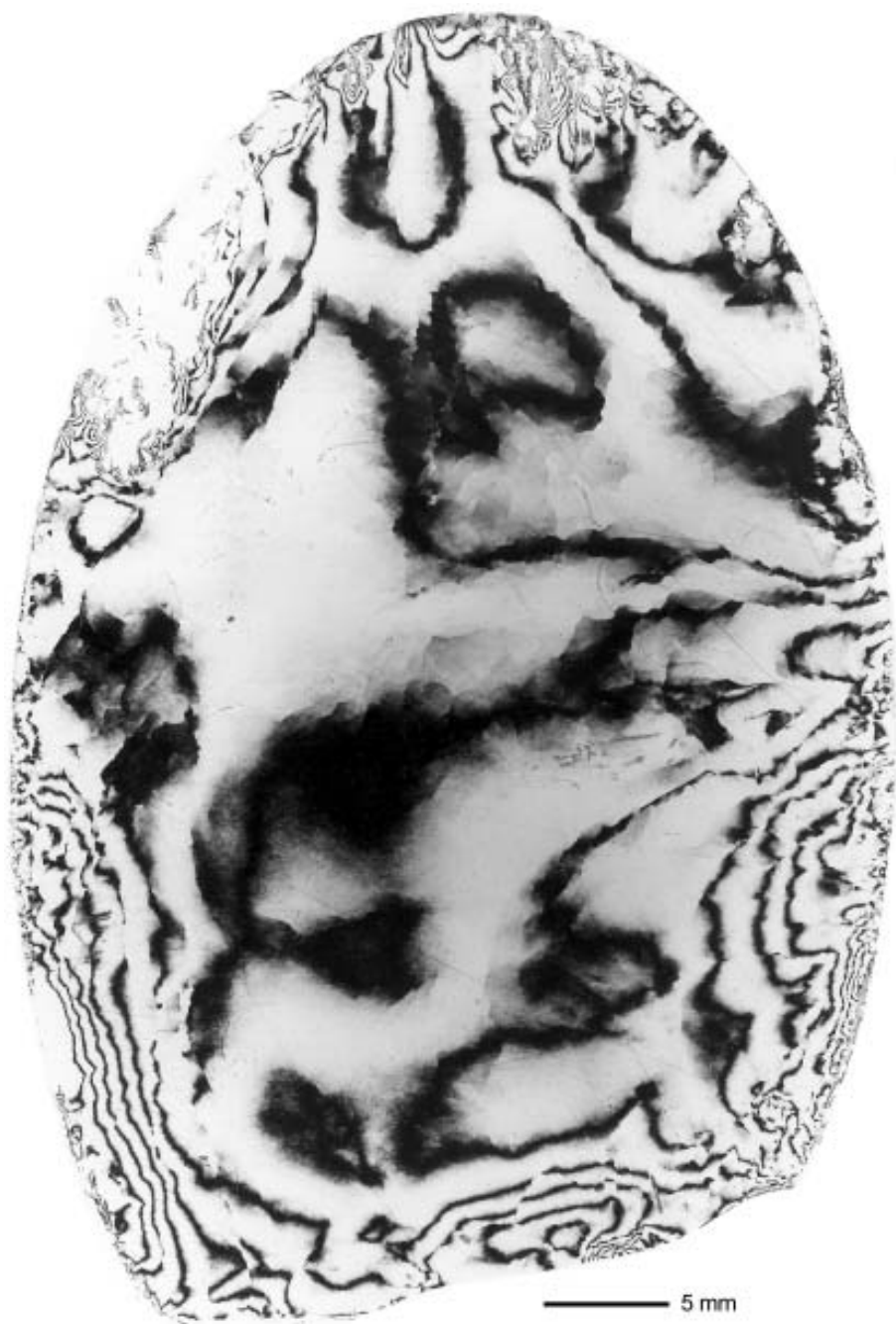
Figure 18. *Diffraction contour mapping of a CdZnTe crystal. The sample Bragg angle was rotated in 0.015° steps. At each angular position, an image was recorded to produce a multiple-exposure composite image of the strain in the sample.*

The standard photographic medium is Ilford* L4 nuclear emulsion, with a nominal thickness of 25 μm, on glass substrates which can be cut to the required size. The grain size is 0.17 μm, which allows subsequent photographic image magnification. The image can be recorded with the film perpendicular to the diffracted beam, yielding the highest spatial resolution at the cost of image foreshortening, or with the film parallel to the sample, providing a one-to-one image with a consequent broadening of the features, as shown in Figure 6.

Two other useful techniques for extracting information from topographs include recording stereo pairs [Armstrong, 1984] and performing diffraction contour mapping [Larson and Black, 1995]. A stereo image of the defect structure in a sample crystal is obtained by recording two images from the same diffraction differing only by a slight rotation, $\approx 10°$, about the diffraction vector [Haruta, 1964]. Contour mapping is used for samples with inhomogeneous strain, where a single diffraction image will cover only a small part of the sample. Multiple exposures, taken at successive angular positions, display the contours of the strain field [Bowen and Tanner, 1998]. An example of such a multiple exposure topograph, called a zebra-stripe image, is shown in Figure 18. This is a multiple-exposure strain-contour topograph from a CdZnTe crystal. The sample was rotated in 0.015° steps, where an image was recorded at each angular position. Broad stripes indicate lower strain and narrow stripes, such as those seen at the edges, indicate severe strain.

8. DATA ANALYSIS AND INTERPRETATION

Data analysis and interpretation of X-ray topographs takes many forms. The product of an XRT experiment is the diffraction image, which is captured on film or on a digital camera. In many practical applications, the images record changes that have occurred in the sample as a result of the process or processes of interest. Such processes can include modifying crystal-growth parameters, changing surface treatments or annealing conditions, varying dopant concentration, examining device growth and operation or thin-film growth, and the application of electromagnetic fields or mechanical testing. Consider the X-ray topographs of 12 sapphire crystals shown in Figure 19. The dislocation structure is markedly different for the two growth methods. The Czochralski-grown crystals contain subgrains, strained grains and dislocation bands. The heat-exchanger-grown crystals contain no subgrains, almost no strain and very low dislocation density. The appearance of additional surface damage can be traced to inadequate sample-handling protocols. Finally, the effectiveness of polishing procedures and the appearance of specific surface defects can be related to the mechanical strength by correlating the topographic evidence for the existence of defects with strength data.

(0006) Symmetric Surface Diffraction

Czochralski Grown [0001]
Growth Direction

Heat Exchanger Method [11$\bar{2}$0]
Growth Direction
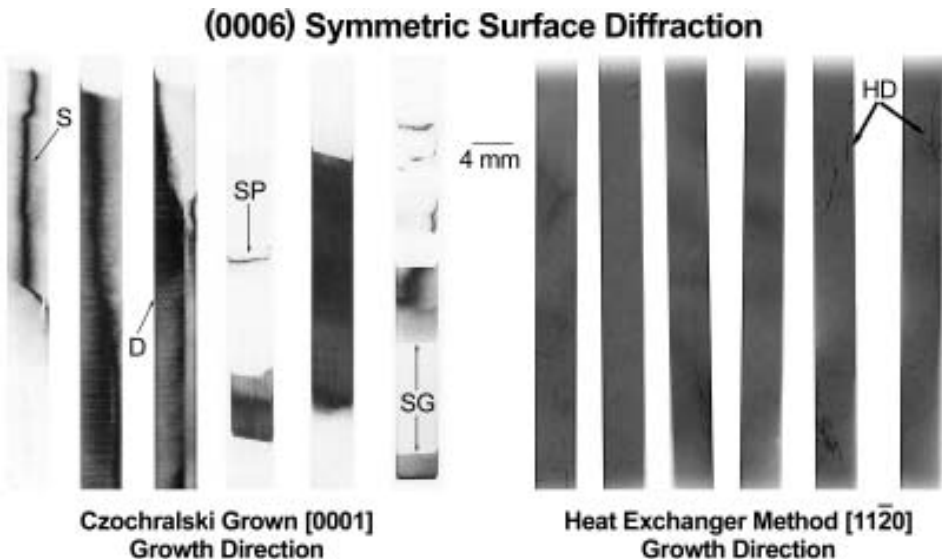
Figure 19. *Surface reflection topographs from 12 sapphire crystals. The microstructure of the six Czochralski-grown crystals consists of subgrains (SG), strained grains showing strain profiles (SP), and dislocation bands (D). The surface also contains residual scratches from fabrication and polishing. The six heat-exchanger-grown crystals contain no subgrains, they are almost strain-free, and they have a very low dislocation density. These crystals show damage to their surfaces from inadvertent mishandling (HD).*
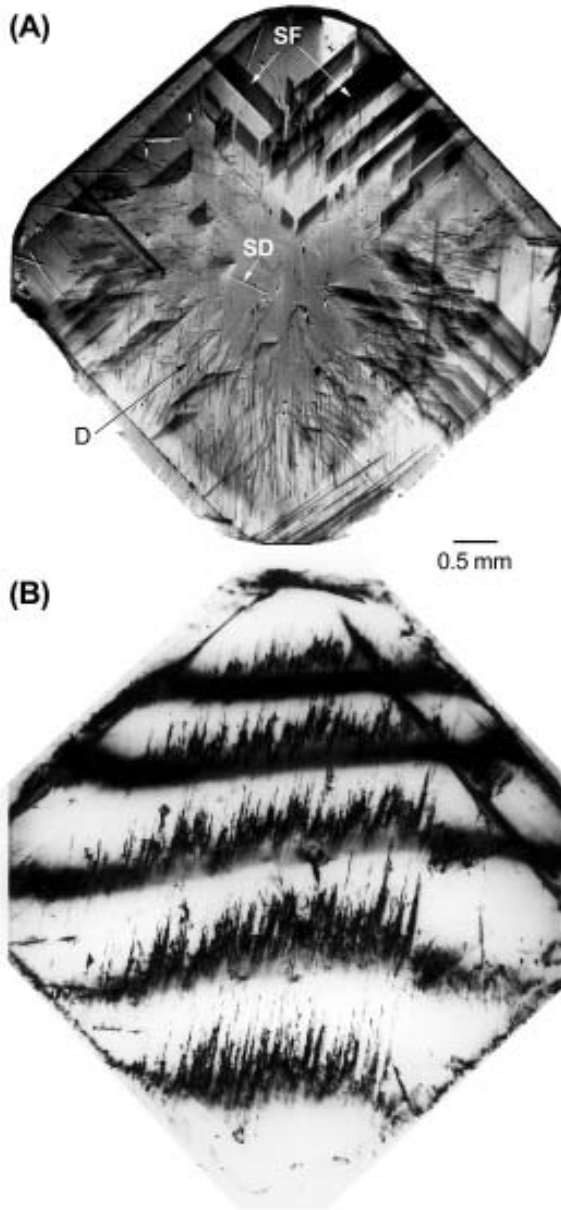
Figure 20. *A transmission topograph from a diamond substrate is shown in (A). This crystal has a distinctive microstructure consisting of stacking faults (SF), dislocations (D), and surface damage (SD). After chemical vapor deposition of a homoepitaxial film, the composite crystal has become extremely strained, as shown in (B). The high defect density of the strained film masks the underlying structure of the substrate. This image is a multiple exposure, using the same procedure as that used to obtain the data in Figure 18, where here the angular steps were 0.04°.*

Rather than attempt an exhaustive description of the data analysis for the wide variety of topographic information that is available, a few selected examples will be shown. A good resource for contemporary XRT experiments and their interpretation can be found in special issues of *Journal of Physics D: Applied Physics* that appeared in 1995 and 1999, in which collections of original papers presented at the biennial conference on High Resolution X-Ray Diffraction and Topography are published.

XRT studies of microstructure development as a function of processing have had significant impact on processing technology. Here an example is given of CVD growth of homoepitaxial diamond. A transmission X-ray topograph of a substrate diamond is shown in Figure 20(A). The data reveal that the substrate crystal contains stacking faults and single dislocations, and there is also a small amount of surface damage. The overall quality, however, is quite good since the microstructure of the entire crystal can be captured in a single monochromatic transmission topograph. Figure 20(B) is a monochromatic transmission topograph taken from the identical crystal and orientation after deposition of a homoepitaxial film equal to the substrate thickness. The composite crystal was so severely strained that the microstructure could not be captured in a single monochromatic transmission topograph. Instead, the image was produced in five exposures, taken 0.04° apart, in the same procedure used to create the contour map shown in Figure 18. The post-deposition data indicate the development of copious dislocation walls and a significant amount of curvature. The defect density and the strain in the film, which is facing the X-ray detector, mask the underlying structure of the substrate. The amount of curvature in the crystal was calculated from the range of Bragg angle over which it diffracts. The sample diffracts over 0.2° along its length of 8 mm, indicating a curvature of about 2.3 m.

The next example is one of dynamic *in situ* topography, in which the dislocation mobility in ice is followed [Xiahong, *et al*., 1995]. The experiments were conducted in real time with the ice crystal under tension. The distance that individual dislocations moved under a known load was used to derive the mobility. A monochromatic transmission topograph of an ice crystal is shown in Figure 21 where the real time data were recorded directly by an X-ray video camera.
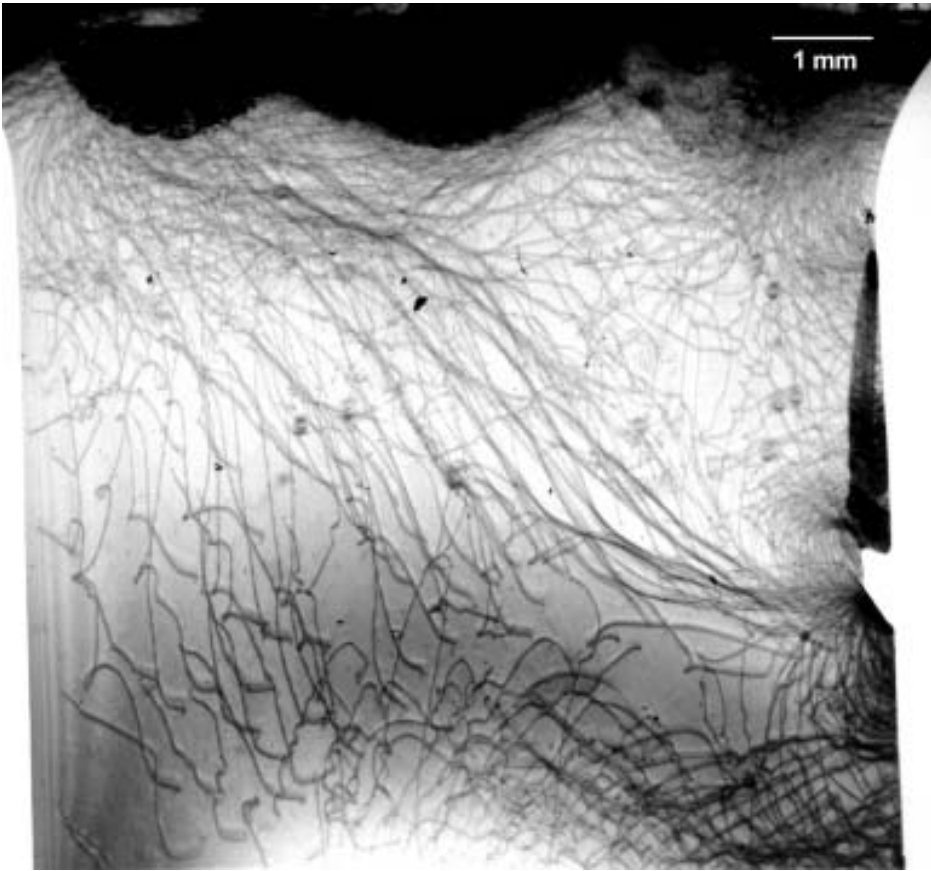
Figure 21. *A transmission topograph through an ice crystal about 1 mm thick. The dislocation mobility can be determined by following the motion of individual dislocation as a function of applied load in real time.*

In another example of *in situ* topography, the formation of dislocation structures in single-crystal aluminum was followed. Figure 22 shows a sequence of ($\bar{2}$20) transmission diffraction images of a 1-mm-thick aluminum crystal, deformed *in situ* to a maximum strain of 1.9%. The sequence shows the evolution of dislocation walls from diffuse intermittent structures at 0.85% strain to sharply defined walls at 1.9% strain. Since these are disruption images, the walls are white against a darker background. The white lines extending from the lower left to the upper right are $\bar{1}\bar{1}1$ dislocation walls, parallel, and the less prominent features on the other diagonal are the $\bar{1}1\bar{1}$ dislocation walls. The $\bar{1}\bar{1}1$ planes are clearly the dominant slip planes for this region of the sample. The bright horizontal lines are actually a series of bright spots. These represent a set of grown-in dislocations that lie on

one of the remaining two slip planes. Information from these images was also used to derive parameters from a complementary experiment, ultra-small-angle X-ray scattering [Levine, *et al.*, 2000]. The scattering experiment was carried out on samples crystallographically identical to the one imaged in Figure 22. Scattering from the interface between the wall and the surrounding material was identified, but it was necessary to know the orientation of the walls with respect to the diffraction vector before the true thickness of the interface could be derived. This information was obtained from the diffraction images in Figure 22.
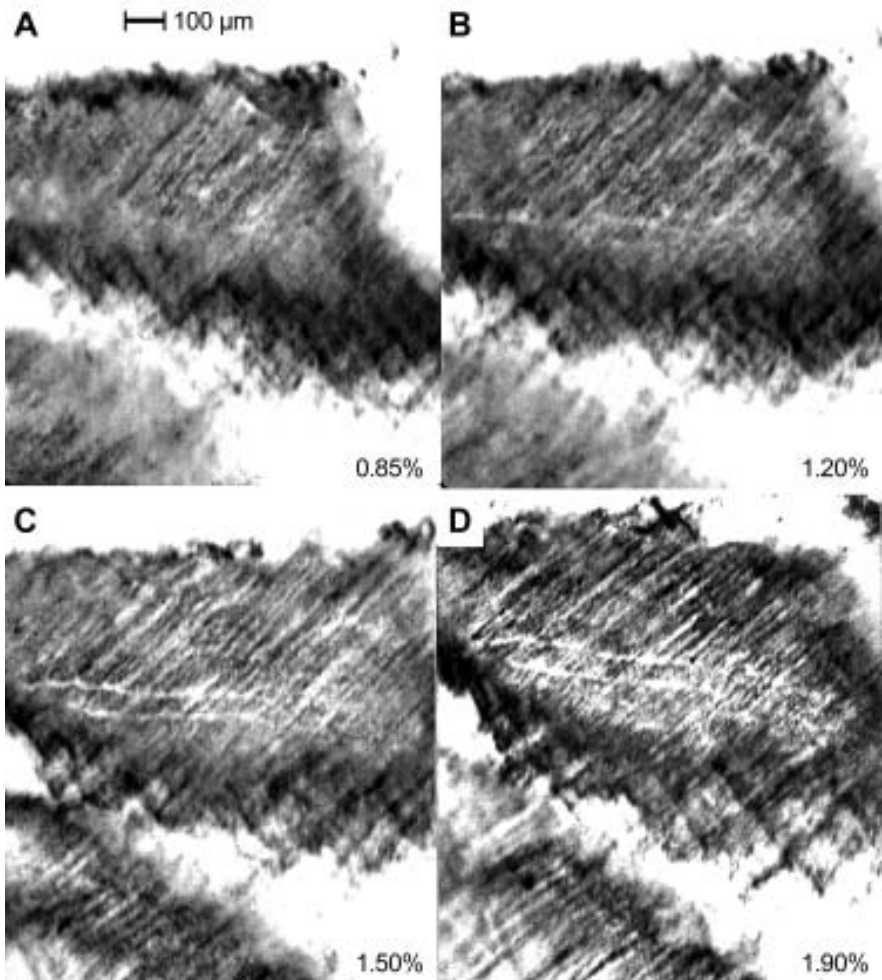
Figure 22. *A series of topographs from an aluminum crystal strained to (A) 0.85%, (B) 1.2%, (C) 1.5%, and (D) 1.91%. The formation of dislocation structures was correlated with ultra-small-angle X-ray scattering data.*
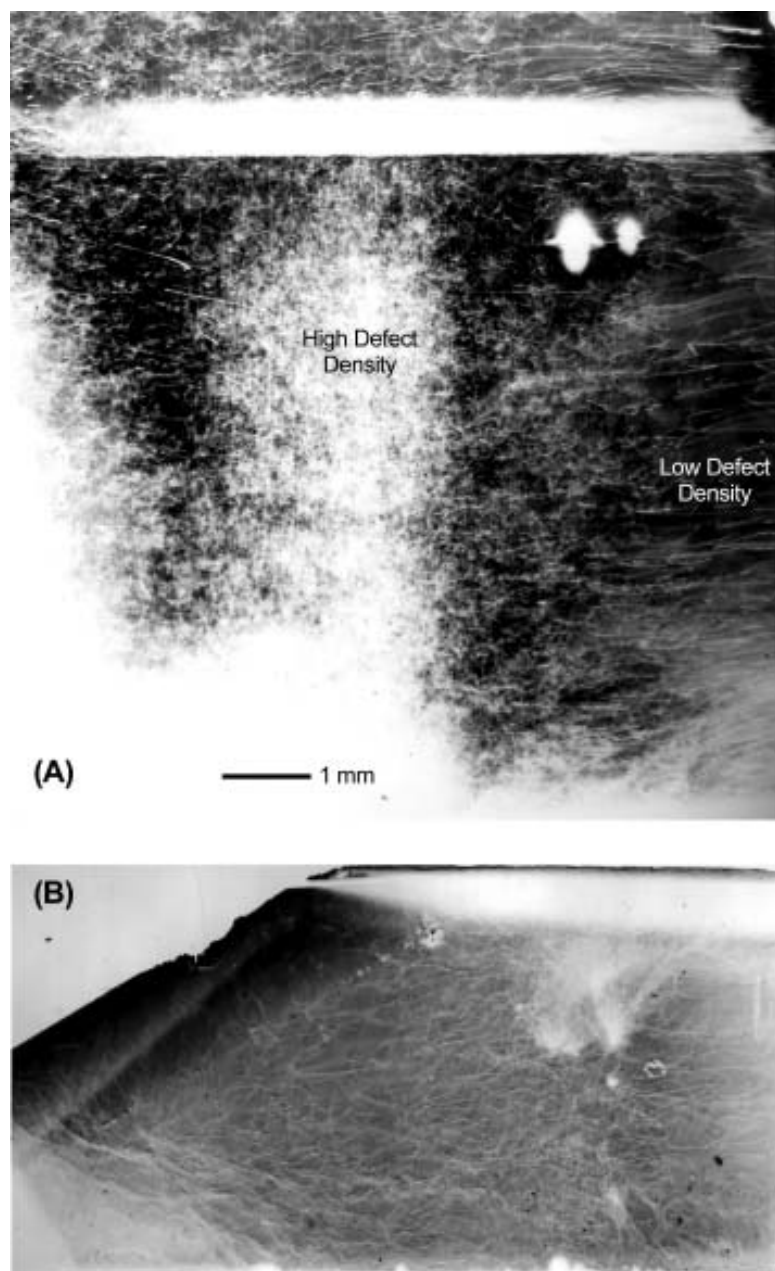
Figure 23. *Anomalous transmission topographs of ZnSe crystals grown by physical vapor transport (PVT) and by grain refinement (GR). The image in (A) from the PVT crystal shows a large variation in dislocation density, to the extent that anomalous transmission does not occur in the central region. A much lower dislocation density is observed at the edge. The sample shown in (B) from the GR crystal has a more uniform distribution of defects and a lower overall dislocation density.*

X-ray topography has contributed significantly to crystal-growth studies. The ability to correlate crystalline imperfections such as growth striations, precipitates and dislocations with growth conditions is essential to the effort to improve crystal quality. In the example given here, ZnSe crystals grown by a grain refinement (GR) process and by physical vapor transport (PVT) are shown in Figure 23. The monochromatic transmission image in Figure 23(A) of the PVT crystal shows a very inhomogeneous microstructure. The central region is so severely defected that the X-ray beam does not make it though the crystal. Outside the strained regions, single dislocations and precipitates are clearly evident. In Figure 23(B), the GR crystal shows both a more uniform distribution and lower density of dislocations.

9. PROBLEMS

The best X-ray topographs display the defect structure of the sample and are free from spurious features that detract from the microstructure of interest. Unfortunately, there are many possible sources of spurious contrast. Of major concern for MXRT, for example, is the quality of the monochromator crystals. If these crystals contain imperfections, the image of those defects may be visible along with the recorded image from the sample, Figure 24. Most often, the images from such defects will be very diffused, compared to the images from the sample defects, because the monochromator is typically much further from the detector than the sample. An obvious method to distinguish between monochromator and sample images is to translate the monochromator crystals or the sample and observe when the features move.
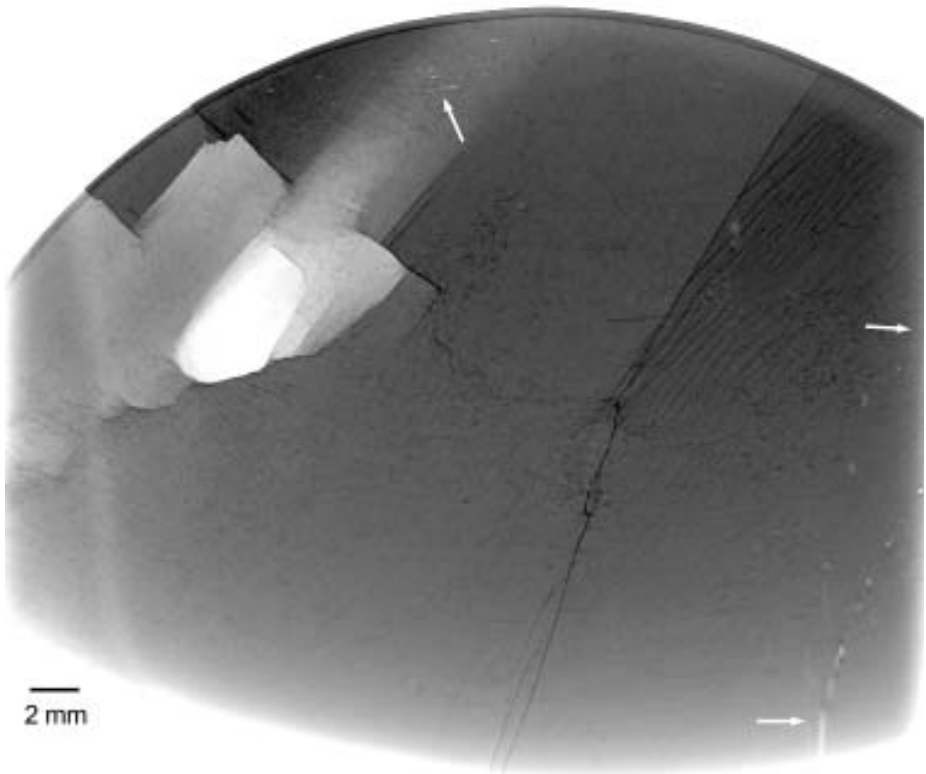

2 mm

Figure 24. *A (00018) reflection topograph from a sapphire dome. Imperfections on the monochromator crystals appear as the fuzzy light features indicated. Subgrain structure in this large crystal is seen on the left and growth related dislocation structures are evident in the upper right.*

Any object in the X-ray beam may produce an image. One object under the control of the experimenter is the material enclosing the photographic film. Often, paper or plastic is used. These sometimes have a texture that produces a fine contrast in the recorded image due to variable absorption.

Another possible source of contrast, this one beyond the experimenters' control, is the vacuum window separating the synchrotron optics from the topography station. These windows may have nonuniform thickness and produce phase images, and/or they can become oxidized or otherwise contaminated over time and cause a diffuse contrast to be seen in all images. An example is shown in Figure 8, where features attributable to a beryllium window are seen alongside dislocation images from the sample.

Another consideration is the size of the incident beam, which should be kept as small as possible and still provide the desired image area. When the beam is larger than the sample, the increased general scatter will reduce the effective image contrast. If the beam impinges on the sample mounting material, there is the possibility of recording diffraction images from individual grains in a polycrystalline mount. An example of this is seen in Figure 15. Here a sapphire sample was as large as the mount, and some of the beam impinged on the aluminum holder. This caused the formation of an aluminum Debye–Sherrer ring along with the microstructure of the sapphire sample. Since the beam was collimated and monochromatic, only a small number of grains diffract producing well-defined images of the grains.

REFERENCES

Authier, A. "Contrast of Images in X-ray Topography." *Modern Diffraction and Imaging Techniques in Material Science*. Ed. S. Amelinckx, R. Gevers, G. Remault and J. Van Landuyt. Amsterdam: North-Holland, 1970.

Authier, A., S. Lagomarsino, and B.K. Tanner, eds. *X-ray and Neutron Dynamical Diffraction Theory and Applications*. New York: Plenum Press, 1996.

Armstrong, R.W. "X-ray diffraction topography description via the stereographic projection." *Application of Topographic Methods to Materials Science*. Ed. S. Weissman, F. Balibar and J.–F. Petroff. New York: Plenum Press, 1984, pp. 33–43.

Barrett, C.S. "A new microscope and its potentialities." *Trans. AIME*, **161**, (1945), 15–64.

Batterman B.W., and H. Cole. "Dynamical diffraction of X-rays by perfect crystals." *Rev. Mod. Phys*., **36**, (1964), 681–717.

Berg, W.F. "Über eine röntgenographische Methode zur Untersuchung von Gittstörungen in Kristallen." *Naturwiss.,* **19**, (1931), 391–396.

Black, D.R., and H.E. Burdette. "Diffusion bonding of ductile single crystals for strain free mounting." *J. Appl. Crystallography,* **19**, (1986), 279.

Boettinger, W.J., H.E. Burdette, and M. Kuriyama. "Observation of oblique magnetic domain walls in nickel single crystals by X-ray topography." *Phil. Mag.,* **36**, (1977), 763–776.

Bonse, U. "X-ray picture of the field of lattice distortions around single dislocations." *Direct Observations of Imperfections in Crystals*. Ed. J.B. Newkirk and J.H. Wernick. New York: Interscience Publishers — John Wiley and Sons, 1962, pp. 431–460.

Borrmann, G. "Über Extinktionsdiagramme von Quarz." *Phys. Zeit.,* **42**, (1941), 157–162.

Borrmann, G., W. Hartwig, and H. Irmler. "Shatten von Verzetzungslinien im Röntgen–Diagramm." *Z. Naturforsch.*, **13a**, (1958), 423–425.

Borrmann, G. "Die hell-dunkel Struktur der Röntgen–Shattenbilder von Verzetzungen." *Physik. Bl.*, **15**, (1959), 508–509.

Bowen, D. Keith, and B. Tanner. *High Resolution X-ray Diffractometry and Topography*. London: Taylor and Francis, 1998.

Capelle, B., Y. Epelboin, and C. Malgrange. "X-ray topographic study of antiphase domain boundaries in ferroelectric ferroelastic GdDy(MoO$_4$)$_3$ crystals." *II. Evaluation of the additional translation vector. J. Appl. Phys.*, **53**, (1982), 6767–6771.

Cloetens, P., W. Ludwig, J. Baruchel, J.–P. Guigay, P. Pernot–Rejmánková, M. Salomé–Pateyron, M. Schlenker, J.–Y. Buffière, E. Maire, and G. Peix. "Hard X-ray phase imaging using simple propagation of a coherent radiation beam." *J. Phys. D: Appl. Phys.*, **32**, (1999), A145–A151.

Cullity, B.D. *Elements of X-ray Diffraction.* Reading: Addison–Wesley, 1967, pp. 118–123.

Epelboin, Y. *DEFW*, *DEF4*, and other programs are available as freeware. World Wide Web, 1999.

Guinier, A., and J. Tennevin. "Sur deux variantes de la méthode de Laue et leurs applications." *Acta Cryst.*, **2**, (1949), 133–138.

Hart, M.J. "Synchrotron radiation—its applications to high-speed, high-resolution X-ray diffraction topography." *Appl. Cryst.*, **8**, (1975), 436–444.

Hart, M. "Elementary dynamical theory." *Characterization of crystal growth defects by X-ray methods*. Ed. B.K. Tanner and D.K. Bowen. New York: Plenum Press, 1980, 216–263.

Haruta, K. "New method of obtaining stereographic pairs of X-ray diffraction topographs." *J. Appl. Phys.*, **76**, (1964), 1789–1790.

Imamov, R.M., A.A. Lomov, and D.V. Novikov. "Grazing Incidence Diffraction X-ray Topography." *Phys. Stat. Sol (A)*, **115**, (1989), K133.

Kato, N. "Statistical Theory of Dynamical Diffraction in Crystal." *X-ray and Neutron Dynamical Diffraction Theory and Applications*. Ed. A. Authier, S. Lagomarsino and B.K. Tanner. New York: Plenum Press, 1996.

Kohra, K., M. Yoshimatsu, and I. Shimizu. "X-ray observation of lattice defects using a crystal monochromator." *Direct Observations of Imperfections in Crystals*. Ed. J.B. Newkirk and J.H. Wernick. New York: Interscience Publishers—John Wiley and Sons, 1962, pp. 461–470.

Kuriyama, M., W.J. Boettinger, and G.G. Cohen. "Synchrotron radiation topography." *Ann. Rev. Mat. Sci.*, **12**, (1982), 23–50.

Kuriyama, M., and G.G. Cohen. "X-ray extinction theory in the Bragg geometry." *Z. Naturforsch.*, **37a**, (1982), 465–473.

Kuriyama, M., and G.G. Long. "Extinction theory in X-ray topography." *Applications of X-Ray Topographic Methods to Materials Science*. Ed. S. Weissmann, F. Balibar and J.–F. Petroff. New York: Plenum Press, 1984, pp. 97–09.

Lang, A.R. "Direct observation of individual dislocations." *J. Appl. Phys.*, **29**, (1958), 597–598.

Lang, A.R. "The projection topograph: a new method in X-ray diffraction microradiography." *Acta Cryst.*, **2**, (1959), 249–250.

Lang, A.R. "Recent Applications of X-ray Topography." *Modern Diffraction and Imaging Techniques in Material Science*. Ed. S. Amelinckx, R. Gevers, G. Remault and J. Van Landuyt. Amsterdam: North-Holland, 1970.

Lang, A.R. "The Properties and Observation of Dislocations." *Crystal Growth: An Introduction*. Ed. P. Hartman. Amsterdam: North-Holland, 1973, pp. 444–512.

Lang, A.R. "Defect Visualization: Individual Defects." *Characterization of Crystal Growth Defects by X-Ray Methods*. Ed. B.K. Tanner and D.K. Bowen. New York: Plenum Press, 1980, pp. 401–420.

Lang, A.R. "Topography." *International Tables for Crystallography*, Volume C, International Union of Crystallography. Dordrecht: Kluwer Academic Publishers, 1992, pp. 113–123, 134–136.

Larson, D., and D. Black. *(Unpublished results.)* 1995.

Levine, L.E., G.G. Long, and D.R. Black. "Complementary Experimental Techniques For Mutli-scale Modeling Of Plasticity," *Multiscale Phenomenon in Materials—Experiment and Modeling*. Ed. B. Devincre, D. Lassila, R. Phillips and I. Robertson. *MRS Symp. Proc.*, **578**, (2000). Warrendale: MRS.

Miltat, J. "White beam synchrotron radiation topography." *Characterization of Crystal Growth Defects by X-Ray Methods*. Ed. B.K. Tanner and D.K. Bowen. New York: Plenum Press, 1980, pp. 401–420.

Newkirk, J.B. "Method for the detection of dislocations in silicon by X-ray extinction contrast." *Phys. Rev.*, **110**, (1958), 1465–1466.

Novikov, D., M. Ohler, R. Köhler, and G. Meterlik. "Observation of defects in crystal surface layers by grazing-incidence diffraction x-ray topography." *J. Phys. D: Appl. Phys.*, **28**, (1995), A84–A87.

Petroff, J.–F. "Basic understanding of image formation in X-ray topography." *Applications of X-ray Topographic Methods to Materials Science*. Ed. S. Weissmann, F. Balibar and J.–F. Petroff. New York: Plenum Press, 1984, pp. 75–96.

Preuss, E., B. Krahl–Urban, and B. Rainer. *Laue Atlas*. New York: John Wiley and Sons, 1973.

Sauvage, M., and J.F. Petroff. "Application of synchrotron radiation to X-ray topography." *Synchrotron Radiation Research*. Ed. H. Winick and S. Doniach. New York: Plenum Press, 1980, pp. 607–638.

Schulz, L.G. "Method of using a fine-focus X-ray tube for examining the surface of a single crystal." *J. Met.*, **6**, (1954), 1082–1083.

Steiner, B., U. Laor, M. Kuriyama, G.G. Long, and R.C. Dobbyn. "Diffraction Imaging of High Quality Bismuth Silicon Oxide with Monochromatic Synchrotron Radiation: Implications for Crystal Growth." *J. Cryst. Growth*, **87**, (1988), 79–100.

Takagi, S. "Dynamical theory of diffraction applicable to crystals with any kind of small distortion." *Acta Cryst.*, **15**, (1962), 1311–1312.

Takagi, S. "A dynamical theory of diffraction for a distorted crystal." *J. Phys. Soc. Jpn.*, **26**, (1969), 1239–1253.

Tanner, B.K. *X-ray Diffraction Topography*. Oxford: Pergammon, 1976.

Tanner, B.K. "Crystal assessment by X-ray topography using synchrotron radiation." *Prog. Cryst. Growth Charact.*, **1**, (1977), 23–56.

Tanner, B.K., and D.K. Bowen, eds. *Characterization of Crystal Growth Defects by X-Ray Methods*. New York: Plenum Press, 1980.

Tanner, B.K. "Contrast of Defects in X-ray Diffraction Topographs." *X-ray and Neutron Dynamical Diffraction Theory and Applications*. Eds. A. Authier, S. Lagomarsino and B.K. Tanner. New York: Plenum Press, 1996.

Taupin, D. "Prévision de quelques images des dislocations par transmission des rayons X (cas de Laue symmétrique)." *Acta Cryst.*, **23**, (1967), 5–35.

Weissman, S., F. Balibar, and J.–F. Petroff. *Applications of X-Ray Topographic Methods to Materials Science*. New York: Plenum Press, 1984.

Xiaohong, H., J. Kunlum, I. Baker and D. Black. "Dislocation Mobility in HCl-Doped Ice." *Application of Synchrotron Radiation Techniques to Materials Science II*. Ed. L. Terminello, N. Shinn, G. Ice, K. d'Amico and D. Perry. *MRS*, Vol. 375, (1995).

Zachariasen, W.H. *Theory of X-Ray Diffraction in Crystals*. New York: John Wiley and Sons, 1945.

April 2004